Detailed and simplified kinetic schemes for high enthalpy air flows and their influence on catalycity studies

Anne Bourdon
Laboratoire EM2C UPR 288 CNRS
Ecole Centrale Paris, Grande voie des vignes
92295 Châtenay-Malabry Cedex, France
email : Anne.Bourdon@em2c.ecp.fr

Arnaud Bultel
UMR CNRS 6614 CORIA
Université de Rouen - Site universitaire du Madrillet - BP12
76801 Saint-Etienne du Rouvray cedex, France
email : Arnaud.Bultel@coria.fr

February 8, 2006

Contents

Bourdon, A.; Bultel, A. (2007) Detailed and Simplified Kinetic Schemes for High Enthalpy Air Flows and Their Influence on Catalycity Studies. In *Experiment, Modeling and Simulation of Gas-Surface Interactions for Reactive Flows in Hypersonic Flights* (pp. 9-1 – 9-60). Educational Notes RTO-EN-AVT-142, Paper 9. Neuilly-sur-Seine, France: RTO. Available from: http://www.rto.nato.int/abstracts.asp.

1 Abstract

The thorough understanding of the formation and the relaxation of the plasma produced in the shock layer developed during the re-entry of a spacecraft in the upper layers of the earth's atmosphere is crucial in order to prevent damaging of its outer surface. Among the different points to be studied, the chemical aspects are particularly important: the mechanical characteristic time scale of the flow being short, the flow is indeed in chemical nonequilibrium. In addition, the inner storage of energy of the different species of the flow leads to other mechanical behaviors than those observed in classical low temperature flows. These nonequilibrium effects have to be taken into account accurately in codes devoted to the study of the interaction between the plasma and the surface.
In this paper, we propose to focus our attention on the detailed kinetics of an air plasma under nonequilibrium conditions. First, we present a time-dependent collisional-radiative (CR) model for atomic oxygen to study in detail ionization and three-body recombination rates of oxygen in high temperature air plasma flows. Second we present a time-dependent CR model for air taking into account 13 species and numerous excited states and working over a wide range of pressure and temperature. For typical conditions encountered in re-entry flows, we compare this detailed CR scheme for air with simplified schemes (proposed by Park, Dunn & Kang and Gupta et al.) usually implemented in high enthalpy air flow codes. Finally, a $1D$ code simulating the stagnation point boundary layer near the wall of the spacecraft is presented and the influence of the gas chemistry on the wall catalycity is discussed.

2 Introduction

During the re-entry of a spacecraft into the upper layers of the atmosphere of a planet, the flow is hypersonic and a shock layer is formed in front of the vehicle (Anderson (1989)). In crossing the shock layer, the flow is hardly slowed down and the gas is strongly heated (up to $15000\,K$ (Carlson and Hassan (1992))) and therefore becomes a plasma. Near the surface, a boundary layer is formed due to the difference between the temperature inside the shock layer and the wall temperature and this induces high energy flux densities to the vehicle surface. These fluxes have to be reduced to prevent damaging of the spacecraft.
To choose correctly the material of the thermal shield it is necessary to study the thermal interaction between the gas medium and the vehicle (Hankey (1994)) and therefore to study thoroughly the plasma formed in the shock layer (i.e. different species concentrations close to the wall, their internal degree of excitation, etc). In the present context, the flow is far from equilibrium; after an ionization phase, the plasma is recombining as it approaches the thermal shield and the velocity is high. As a result, the chemistry is time-dependent in the frame of the moving plasma. Its calculation needs an accurate kinetic scheme. Moreover, as the pressure varies over a wide range during the re-entry phase, the kinetic scheme has to take into account a sufficient number of binary and ternary collisions. Currently, despite the large number of experimental and theoretical studies on high temperature air chemistry, uncertainties remain on the accuracy of numerous reaction rates.
In particular, the effective ionization and recombination rates of atoms are difficult to

determine experimentally and, then most available results have been derived from theoretical studies. However, a reaction such as $O^+ + 2e^- \leftrightarrow O + e^-$ results from numerous different elementary processes between the atomic levels of oxygen. Therefore, the accuracy of theoretical effective ionization and recombination rate coefficients depends on the choice of the atomic model and on the choice of the rate coefficients for the elementary processes. In section 3, we present a time-dependent collisional radiative model for atomic oxygen in order to determine effective ionization and recombination rate coefficients for $10^{18}m^{-3} \leq n_e \leq 10^{21}m^{-3}$ and $8000K \leq T_e \leq 20\,000K$. We will show that a time-dependent approach allows to follow the relaxation of atomic level populations and to study the validity of the quasi-steady-state hypothesis.
As far as we know, no time-dependent collisional-radiative model dedicated to re-entry applications exists for air, taking into account N_2, O_2, NO, N, O, N_2^+, O_2^+, NO^+, N^+, O^+, O_2^-, O^- on their ground state and on numerous electronic excited states. Although some collisional-radiative models have been earlier elaborated by Teulet et al. (2001) and Sarrette et al. (1995), no model works between $1\,kPa$ and the atmospheric pressure. In addition, considerable improvements have been made about data in term of excitation by electron impact, dissociative recombination of NO^+, O_2^+ and N_2^+ and their branching fractions as well as vibrational processes. In section 4, we propose to focus on two important points in the case of the plasma formed during the re-entry into the earth's atmosphere: (1) the time-dependent chemistry of an ionizing or recombining air plasma and (2) the comparison with existing simplified kinetic schemes used up to now in Navier-Stokes codes. This study is based on the elaboration of a time-dependent collisional-radiative model for heavy particles temperature T_A and electron temperature T_e less than $10000\,K$. The results of the elaborated CR model are finally discussed for different re-entry conditions.
Finally, in section 5, we present the influence of the choice of the kinetic scheme for air on the wall heat flux on a TPS material in the stagnation point boundary layer for different conditions.

3 Collisional-radiative model for O atoms

In this section, we propose to set up a collisional radiative model for atomic oxygen in order to determine effective ionization and recombination rate coefficients for $10^{18}m^{-3} \leq n_e \leq 10^{21}m^{-3}$ and $8000K \leq T_e \leq 20\,000K$. In an earlier study, Taylor and Ali (1986) determined these rate coefficients for slightly different conditions: $10^{22}m^{-3} \leq n_e \leq 10^{25}m^{-3}$ and $1eV \leq T_e \leq 3eV$. Other previous collisional radiative models for oxygen have been devoted to the study of the population densities at the stationary state (Gomès et al. (1990); Soon and Kunc (1990)) and relaxation times (Cacciatore and Capitelli (1976)). Since the study of Taylor and Ali, numerous experiments and computations have been carried out to improve the accuracy of atomic cross sections and Einstein coefficients in oxygen. In this work, we have tried to determine the best possible coefficients available in the literature. The data critically compiled by Soon and Kunc (1990) have been used with a few updates on $e-$O inelastic collisions (Doering (1992)) and on Einstein coefficients (Biémont and Zeippen (1992); Bhatia and Kastner (1995)). In this study, we consider a spatially uniform and electrically neutral plasma. We assume that the distributions of energies of particles are Maxwellian and that the atom-atom and ion-atom inelastic

collisions are negligible. The treatment of radiation is limited to either optically thin or optically thick cases.
Unfortunately, no experimental data are available on the effective ionization and recombination rates of atomic oxygen to compare with our results. In high temperature air kinetic schemes used in plasma flow codes, different analytical expressions, which accuracy is unknown, are proposed for these rate coefficients (Park (1990); Gupta et al. (1990); Losev et al. (1994)). Therefore, this work is the opportunity to study the validity of these simple analytical expressions for the effective ionization and recombination rates of atomic oxygen. Furthermore, the time-dependent approach used in this paper allows us to follow the relaxation of atomic level populations and to study the validity of the quasi-steady-state hypothesis.

3.1 Atomic model

In this work, forty coalesced energy levels of the neutral oxygen atom have been considered (Moore (1993)). Their characteristics (for each level index: level configuration, energy and statistical weight) are given in Table 1. As in the nitrogen atom, there is a large energy gap in the oxygen atom between the two first metastable levels ($2s^2 2p^4\ ^1$D and $2s^2 2p^4\ ^1$S) and the other excited levels which lie in a narrow region of energy. However, it is interesting to note that in the oxygen atom, the resonant level is only the fifth level, located at 9.52 eV from the ground state. In their atomic model for oxygen, Soon and Kunc (1990) considered only the nine first levels of our model. In this case, the last level lies 1.69 eV under the ionization limit. With our model, this energy gap is only of 0.124 eV. The influence of the atomic model on the results will be discussed in the following sections. In the electron temperature range of our study, we consider only the ground ionic term of O^+, $2s^2 2p^3\ ^4$S (13.62 eV) which is taken as the "core" for all atoms. Processes involving O^- ions could *a priori* also influence the determination of the ionization and recombination rate coefficients. However, Soon and Kunc (1991) showed that for $T_e \geq 8000K$, the contribution of O^- ions to production of electrons, positive ions and excited atoms is negligible. Therefore, in this study, the influence of O^- ions has been neglected.

3.2 Elementary rate coefficients

In a uniform plasma, the evolution of the population density of an excited atomic level i is due to different elementary processes

$$O_i + e^- \rightleftharpoons O_j + e^- \quad \text{for } i < j \qquad [C_{ij}, C_{ji}] \tag{1}$$

where C_{ij} (m^3 s^{-1}) and C_{ji} (m^3 s^{-1}) are, respectively, the electron-impact excitation rate coefficient for the transition from the level i to the level j and its inverse deexcitation rate coefficient

$$O_i + e^- \rightleftharpoons O^+ + 2e^- \qquad [\beta_{ic}, \beta_{ci}] \tag{2}$$

where β_{ic} (m^3 s^{-1}) and β_{ci} (m^6 s^{-1}) are, respectively, the electron impact ionization rate coefficient from the level i and the three-body recombination rate coefficient on the same level

$$O_j \longrightarrow O_i + h\nu \quad \text{for } i < j \qquad [A_{ji}] \tag{3}$$

i	$1s^2 +$	$E_i(eV)$	g_i
1	$2s^2 2p^4(^3P)$	0.000	9
2	$2s^2 2p^4(^1D)$	1.970	5
3	$2s^2 2p^4(^1S)$	4.190	1
4	$2s^2 2p^3 3s(^5S^o)$	9.150	5
5	$2s^2 2p^3 3s(^3S^o)$	9.520	3
6	$2s^2 2p^3 3p(^5P)$	10.740	15
7	$2s^2 2p^3 3p(^3P)$	10.990	9
8	$2s^2 2p^3 4s(^5S^o)$	11.840	5
9	$2s^2 2p^3 4s(^3S^o)$	11.930	3
10	$2s^2 2p^3 3d(^5D^o)$	12.090	25
11	$2s^2 2p^3 3d(^3D^o)$	12.100	15
12	$2s^2 2p^3 4p(^5P)$	12.300	15
13	$2s^2 2p^3 4p(^3P)$	12.370	9
14	$2s^2 2p^3 3s'(^3D^o)$	12.550	15
15	$2s^2 2p^3 5s(^5S^o)$	12.670	5
16	$2s^2 2p^3 5s(^3S^o)$	12.710	3
17	$2s^2 2p^3 3s'(^1D^o)$	12.740	5
18	$2s^2 2p^3 4d(^5D^o)$	12.760	25
19	$2s^2 2p^3 4d(^3D^o)$	12.770	15
20	$2s^2 2p^3 4f(^5F, {}^3F)$	12.780	56
21	$2s^2 2p^3 5p(^5P)$	12.860	15
22	$2s^2 2p^3(^3P)$	12.890	9
23	$2s^2 2p^3 6s(^5S^o)$	13.030	5
24	$2s^2 2p^3 6s(^3S^o)$	13.050	3
25	$2s^2 2p^3 5d(^5D^o, {}^3D^o)$	13.080	40
26	$2s^2 2p^3 5f(^5F, {}^3F)$	13.087	56
27	$2s^2 2p^3 6p(^5P)$	13.130	15
28	$2s^2 2p^3 6p(^3P)$	13.140	9
29	$2s^2 2p^3 7s(^5S^o)$	13.220	5
30	$2s^2 2p^3 7s(^3S^o)$	13.230	3
31	$2s^2 2p^3[6d(^5D^o, {}^3D^o)$ $+6f(^5F, {}^3F)$ $+6g(^5G^o, {}^3G^o)]$	13.250	168
32	$2s^2 2p^3 8s(^5S^o)$	13.330	5
33	$2s^2 2p^3 8s(^3S^o)$	13.340	3
34	$2s^2 2p^3[7d(^3D^o, {}^5D^o)$ $+7d(^5F, {}^3F)]$	13.353	96
35	$2s^2 2p^3 9s(^3S^o)$	13.412	3
36	$2s^2 2p^3 8d(^5D^o, {}^3D^o)$	13.418	40
37	$2s^2 2p^3 10s(^3S^o)$	13.459	3
38	$2s^2 2p^3 9d(^3D^o)$	13.464	15
39	$2s^2 2p^3 11s(^3S^o)$	13.493	3
40	$2s^2 2p^3 10d(^3D^o)$	13.496	15
41 (O^+ ion)	$2s^2 2p^3(^4S^o)$	13.620	4

Table 1: Atomic level model.

where A_{ji} (s^{-1}) is the transition probability (Einstein coefficient) from the level j to the level i; and

$$O^+ + e^- \longrightarrow O_i + h\nu \qquad \left[\alpha_i^{RR}, \alpha_i^{RD}\right] \tag{4}$$

where α_i^{RR} (m^3 s^{-1}) and α_i^{RD} (m^3 s^{-1}) are, respectively, the radiative and dielectronic recombination rate coefficients on the level i. Dielectronic recombination is the result of a two-stage process

$$O^+ + e^- \longrightarrow O^* \longrightarrow O_i + h\nu \tag{5}$$

where O^* represents an autoionizing state of the O atom.

3.2.1 Electron-impact excitation and deexcitation rate coefficients

Currently, no complete set of precalculated cross sections exists for oxygen. Therefore, for low atomic levels, measurements of cross sections have been used, when available. For the $1 \rightarrow j \leq 7$ transitions, the cross sections measured by Doering et al. (Doering and Gulcicek (1989b), Doering and Gulcicek (1989a), Gulcicek et al. (1988) and Gulcicek and Doering (1988)) have been used in agreement with the discussion of Soon and Kunc (1990). For the 1→2 transition, it is interesting to note that the shape and magnitude of the cross section have been confirmed recently by Doering (1992). For the $1 \rightarrow 9 \leq j \leq 19$ transitions, the theoretical and experimental cross sections reviewed by Laher and Gilmore (1990) have been used. For all the other transitions, excitation cross sections have to be determined theoretically. In this work, we have used for low atomic levels the Vainshtein formalism which is certainly more adapted than hydrogenic models retained in earlier studies. It would be interesting to use cross sections obtained with more accurate quantum mechanical methods such as close-coupling and R-matrix methods. But these methods are computer intensive, and have been completed, up to now, only for a few systems (Pradhan (1988)). For "difficult" transitions (i.e., involving two atomic electrons), a binary-encounter approximation is used. All details are given in the paper of Soon and Kunc (1990). For atomic levels close to the continuum, all atoms are almost hydrogenic. Therefore, the formalism initially developed for hydrogen by Gryzinski (1965) is used for these levels, and is no doubt more adapted than the Vainshtein formalism.
The use of different theoretical models may result in abrupt changes in the elementary rate coefficient values. In order to eliminate this anomaly, already mentioned in other plasma studies (Park (1971)) we introduce, in the same way, a correction factor such that elementary rate coefficient values vary smoothly from one model to the other. As an example Fig. 1 shows the rate coefficient for the $1 \rightarrow j$ transition. Reliable rate coefficients based on the review of Laher and Gilmore (1990) are available up to $j = 19$. Gryzinski rate coefficients up to $j = 19$ have higher values but we note that in both cases, the rate coefficient decreases rapidly up to $j = 10$ and decreases more slowly for higher values. Therefore, in our model, rate coefficients for $1 \rightarrow j > 19$ are derived using the Gryzinski rate coefficients scaled using the rate coefficient of the $1 \rightarrow 19$ transition. We have checked that discrepancies on the effective ionization and recombination rate values due to this correction remain within a factor of 2.

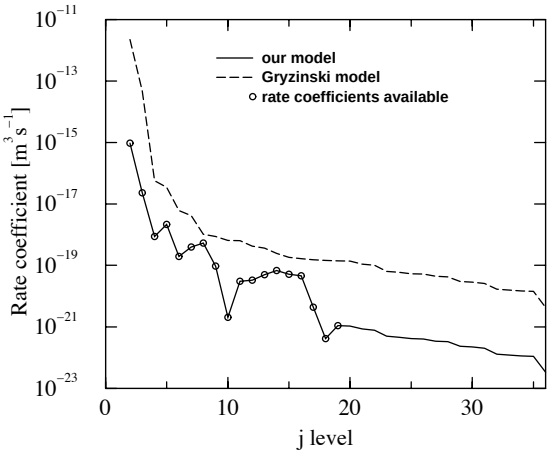

Figure 1: Rate coefficients of the $1 \rightarrow j$ transitions. Open circles: theoretical and experimental rate coefficients reviewed by Laher and Gilmore (1990). Dashed line: Gryzinski (1965) rate coefficients. Solid line: our model.

3.2.2 Electron-impact ionization and three-body recombination rate coefficients

For the ground state and the two lowest excited levels, the models retained by Soon and Kunc (1990) are used. For the other atomic levels, we have used the classical model approximation derived by Gryzinski and Kunc (1986).

3.2.3 Spontaneous emission

For excited levels the energy of which is less than or equal to 11.93 eV, the transitions and the Einstein coefficients reviewed by Soon and Kunc are used. However, for the 5→1 and 9→1 transitions, the Einstein coefficients determined recently by, respectively, Biémont and Zeippen (1992), and Bhatia and Kastner (1995) have been used. For transitions issuing from levels lying higher than 11.93 eV, the best possible Einstein coefficients available in the literature have been used (Bhatia and Kastner (1995); Fuhr and Wiese (1990); Tayal and Henry (1989); Doering et al. (1985); Verner et al. (1996)).

3.2.4 Radiative and dielectronic recombinations

The analytical expressions proposed by Nussbaumer and Storey (1983) are used to calculate the dielectronic recombination coefficients for the effective (direct plus cascade) transitions to the terminating levels i =1 and 4. The total dielectronic recombination rate is

$$\alpha^{RD} = \sum_{i=1,4} \alpha_i^{RD} \tag{6}$$

As in nitrogen, radiative recombination coefficients are significant only for the effective transitions to the three first atomic levels. Using the same approach as Soon and Kunc

(1990), we have calculated and fitted the associated total radiative recombination rate, and obtained

$$\alpha^{RR} = \sum_{i=1}^{3} \alpha_i^{RR} = 2.12 \times 10^{-18} T_e^{-0.29} \ \mathrm{m^3\,s^{-1}} \tag{7}$$

3.3 Master equations

Taking into account the different elementary processes mentioned above, the rate equations for the production of an excited atom on the level i can be written as

$$\frac{dN_i}{dt} = \dot{N}_i = \sum_{j \neq i} n_e N_j C_{ji} + \sum_{j>i} N_j A_{ji} \kappa_{ji} + n_e N^+ \left[\alpha_i^{RR} \kappa_i^{RR} + \alpha_i^{RD} \kappa_i^{RD} + n_e \beta_{ci}\right] - N_i \left[\sum_{j \neq i} n_e C_{ij} + \sum_{k<i} A_{ik} \kappa_{ik} + n_e \beta_{ic}\right] \tag{8}$$

for $1 \leq i \leq np$, where np is the total number of atomic levels, n_e ($\mathrm{m^{-3}}$) the electron number density, N_i ($\mathrm{m^{-3}}$) the population density of the atomic level i, and N^+ ($\mathrm{m^{-3}}$) the number density of O^+. For the escape factors denoted κ_{ij}, κ_i^{RR} and κ_i^{RD}, respectively, for bound-bound, free-bound, and dielectronic radiation, we consider only the limit cases where they are equal either to 0 (optically thick plasma) or to 1 (optically thin plasma). The rate equation for the production of electrons is

$$\frac{dn_e}{dt} = \dot{n}_e = \sum_i n_e N_i \beta_{ic} - \sum_i n_e^2 N^+ \beta_{ci} - \sum_i n_e N^+ \left[\alpha_i^{RR} \kappa_i^{RR} + \alpha_i^{RD} \kappa_i^{RD}\right] \tag{9}$$

Finally, the electrical neutrality of the plasma imposes $n_e = N^+$. We denote $N_a = \sum N_i$, the total atomic density and $N_t = N_a + N^+$, the total particle density. The system of differential equations [Eqs. (8) and (9)] has been integrated numerically in using LSODE Hindmarsh (1980). In each set of calculations, T_e and N_t are constant.

3.4 Results

3.4.1 General behaviour of time-dependent population densities

Figure 2 shows the temporal evolution of the level populations for a typical recombining situation at $t = 0$ s: $n_e = 10^{22} m^{-3}$, $T_e = 12\,000 K$, and $b_i = N_i/N_i^* = 10^{-4}$, where N_i^* is the Saha density of level i. The plasma is considered to be optically thin and all the elementary processes described above are considered. This example clearly puts forward that different time scales characterize the global relaxation process. For $t < 10^{-10}$ s, in this example, N_1, N_2, N_3 and n_e vary only slightly in comparison to other excited state population densities. For $5 \times 10^{-9} s \leq t \leq 10^{-6} s$, the latter reach a plateau whereas N_1, N_2, N_3 and n_e vary significantly. Finally, all the system tends toward a stationary state (reached at $t \simeq 10^{-3} s$ in this example). It is interesting to note that the populations of excited states at the plateau are very different from those at the stationary state. It is important to mention that the general characteristics of the results are independent of the initial ionizing or recombining condition.

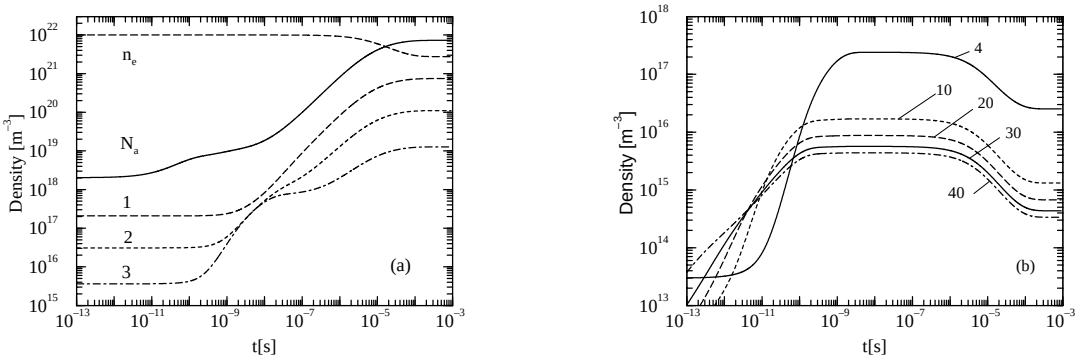

Figure 2: Temporal evolution of densities for an initial recombining situation: at $t = 0$ s, $T_e = 12\,000$ K, $n_e = 10^{20}\mathrm{m}^{-3}$, and $b_i = N_i/N_i^* = 10^{-4}$, where N_i^* is the Saha density of level i. All elementary processes are taken into account, and the plasma is considered to be optically thin. Numbers denote atomic level numbers. Atomic level population densities are divided by their statistical weights.

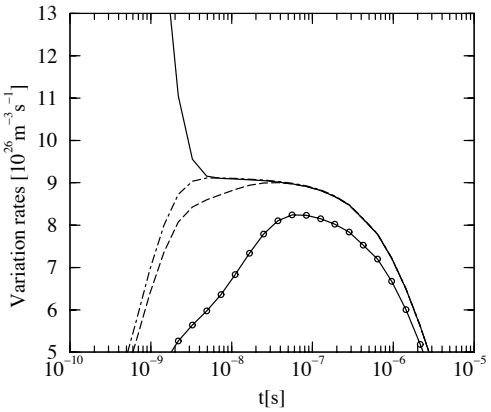

Figure 3: For the same initial recombining condition as in Figure 2. Solid line: $|\dot{n_e}|$. Solid line with open circles: $\dot{N}_1$. Dashed line: $\dot{N}_1 + \dot{N}_2$. Dot-dashed line: $\dot{N}_1 + \dot{N}_2 + \dot{N}_3$.

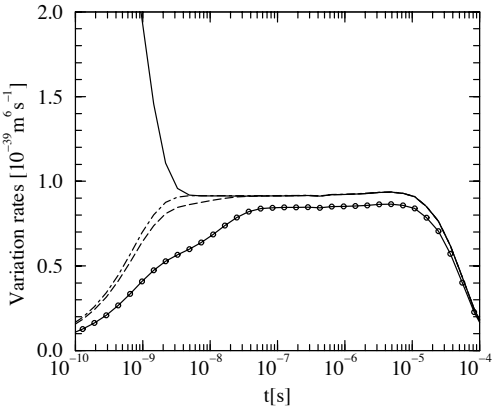

Figure 4: For the initial recombining condition of Fig. 2. Solid line: $|\dot{n_e}|/n_e^3$. Solid line with open circles: $\dot{N}_1/n_e^3$. Dashed line: $(\dot{N}_1 + \dot{N}_2)/n_e^3$. Dot-dashed line: $(\dot{N}_1 + \dot{N}_2 + \dot{N}_3)/n_e^3$.

Figure 3 shows the temporal evolutions of $|\dot{n_e}|$ and $\dot{N}_i$ for 1$\leq i \leq$3. For t $\geq \tau_{min}$ ($\tau_{min} \simeq 5\times10^{-9}$s in this example), we have

$$\dot{N}_i \simeq 0 \quad \text{for} \quad i > 3 \tag{10}$$

and then a quasi-steady-state condition of the form

$$|\dot{n_e}| = \sum_{i=1}^{3} \dot{N}_i \tag{11}$$

can be written. This condition has been already established by Cacciatore and Capitelli (1976) in oxygen. For hydrogen as shown by Bates et al. (1962), the corresponding quasi-steady-state condition takes into account only the ground state of the atom. In oxygen and also in nitrogen as shown by Bourdon and Vervisch (1996), it is necessary to take into account the contribution of the two first low-lying levels. In oxygen, the fourth level is metastable too and then one could have expected to have for oxygen a quasi-steady-state (QSS) condition of the form

$$|\dot{n_e}| = \sum_{i=1}^{4} \dot{N}_i \tag{12}$$

In the electron temperature and density range of our study, we have checked that Eq. (11) is the quasi-steady-state condition for oxygen.

3.4.2 General method to determine effective ionization and recombination rate coefficients

For the global reaction $O^+ + 2e^- \leftrightarrow O + e^-$, we define k_r, the effective three-body recombination rate coefficient, and k_i, the effective ionization rate coefficient, such that

$$\frac{dn_e}{dt} = \dot{n_e} = k_i n_e N_a - k_r n_e^3 \tag{13}$$

Both rate coefficients have to be time independent, but may depend on electron temperature and densities. To determine k_r, the method is to consider at t =0 s a recombining situation. In this case, in early times the first term on the right hand side of Eq. (13) is far much smaller than the second one. Then, if k_r exists, there is a plateau in the temporal evolution of the ratio $|\dot{n_e}|/n_e^3$ and k_r is the value of this ratio at the plateau. Conversely, to determine k_i, one has to consider at t =0 s an ionizing condition and to study the temporal evolution of the ratio $\dot{n_e}/(n_e N_a)$. k_i is the value of this ratio at the plateau. For the initial recombining situation of the last section, Fig. 4 shows that a value of k_r can be determined for $\tau_{min} \leq t \leq \tau_{max}$, with $\tau_{max} \simeq 10^{-5}s$. The minimal time τ_{min} corresponds to the necessary time to reach a quasi-steady-state (Figs. 2 and 3) and is denoted τ_{QSS} in the following. For $t > \tau_{max}$, ionization processes become significant and then the first term on the right hand side of Eq. (13) is no longer negligible in comparison to the second one. Finally, Fig. 3 clearly shows that a quasi-steady-state condition has to be reached to determine k_r. In the case of an initial ionizing situation, the general

characteristics of the results are the same.
Finally, to determine k_r, respectively k_i, we start from an initial recombining, respectively ionizing situation, and, stop the calculations when $|\dot{n}_e|$ and $|\dot{N}_1 + \dot{N}_2 + \dot{N}_3|$ agree to within 1%. Then we determine τ_{QSS} and the value of k_r, respectively k_i, with the instantaneous values of $\dot{n}_e$, and n_e^3, respectively $n_e N_a$. The interest of this approach is the possibility to follow the temporal evolutions of populations and to determine also τ_{QSS}.
It is interesting to point out that ionization and recombination rate coefficients are not independent. Indeed, at the stationary state of the reaction $O^+ + 2e^- \leftrightarrow O + e^-$, the two terms on the right hand side of Eq. (13) have to balance to give $\dot{n}_e = 0$. Then, k_i can be derived from k_r by

$$k_i = k_r \frac{[n_e^{stat}]^2}{N_a^{stat}} = k_r K^{stat} \tag{14}$$

We have checked that both methods gave the same results.

3.4.3 Determination of effective three-body recombination rate coefficients

Optically thick cases
In order to represent an optically thick medium, in this section, all escape factors in Eqs. (8) and (9) are set equal to zero. Then, as only elementary collisional processes are considered, the results of this section are denoted with the superscript C. It is interesting to note that these results may be applied to optically thin media where the electron number density is high enough to neglect radiative processes in comparison to collisions. After having considered different initial conditions, we have pointed out that in an optically thick medium, the three-body recombination rate coefficient for oxygen depends only on the electron temperature (Fig. 5). We have noted no influence of either densities or initial distribution on atomic levels. The simplest best-fit curve for our computed result is

$$k_r^C = 1.32 \times 10^{-39} \left(\frac{T_e}{10^4} \right)^{-4.66} m^6 s^{-1} \tag{15}$$

for 8000 K$\leq T_e \leq$ 20 000 K. Park (1990) assumed that the three-body recombination rate of oxygen is the same as the one of nitrogen, derived for 4000 K$\leq T_e \leq$ 20 000 K in using for all levels the elementary rates derived by Gryzinski (1965) for hydrogen

$$k_{rPark} = 1.15 \times 10^{-38} \left(\frac{T_e}{10^4} \right)^{-5.27} m^6 s^{-1} \tag{16}$$

Figure 5 shows that, over the whole temperature range of this study, the value obtained with our model is on the average five times smaller than the one proposed by Park. With our method, we have also calculated the effective three-body recombination rate coefficient (denoted k_r^H) obtained when one uses for all levels the elementary rates derived by Gryzinski (1965) for hydrogen. In this case, Fig. 5 shows that the value of k_r^H is close to the one proposed by Park. Cacciatore and Capitelli (1976) proposed to modify the elementary rate coefficients derived by Gryzinski to take into account that low-lying levels of atomic oxygen are nonhydrogenic. That is, Gryzinski values are multiplied by a factor 4 for the ground state. It is interesting to mention that this correction has no influence on the calculated value of k_r^H for atomic oxygen. Finally, on Fig. 5, the

fitting law of the three-body recombination rate of nitrogen obtained in a similar work on a collisional-radiative model for atomic nitrogen is represented. This law is given for $4000K \leq T_e \leq 12\,000K$ and, therefore should be handle with care for $T_e > 12\,000K$. However, it is interesting to note that three-body recombination rates for oxygen and nitrogen remain close to each other for $8000K \leq T_e \leq 20\,000K$.

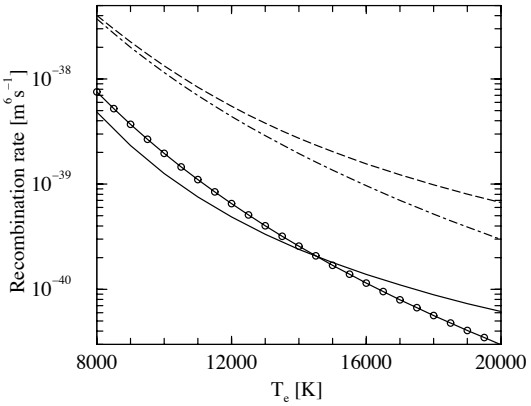

Figure 5: Recombination rate in optically thick cases as a function of T_e. Solid line: our model. Dot-dashed line: Park (1990). Dashed line: our atomic model with Gryzinski (1965) cross sections. Solid line with open circles: Recombination rate of nitrogen (Bourdon and Vervisch (1996)).

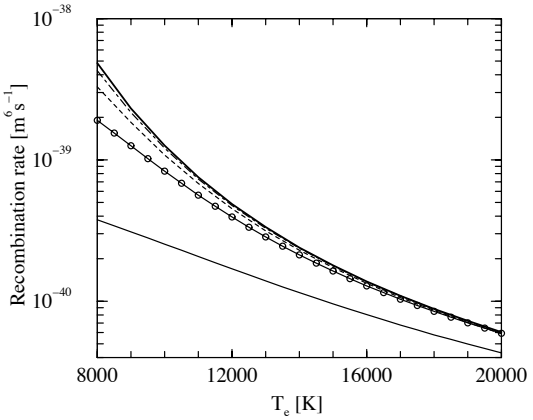

Figure 6: Recombination rate in optically thick cases as a function of T_e. Thick solid line: our 40 level model. Thin solid line: 9 levels. Solid line with open circles: 15 levels. Dashed line: 20 levels. Dot-dashed line: 30 levels.

Influence of the number of levels

Figure 6 shows the influence of the number of atomic levels on the calculated effective three-body recombination rate coefficient value in optically thick cases. As the number of atomic levels increases, the calculated recombination rate converges towards an upper limit and the lower the electron temperature is, the more numerous atomic levels are required to determine k_r^C. This figure puts forward clearly that the 9-level model proposed by Soon and Kunc (1990) is unadapted to our temperature range and that it was necessary to consider a more sophisticated atomic model. Our forty level model appears to be a good compromise between the inaccuracy of atomic models for highly excited levels and the reliability of the effective rate coefficients derived in this study. It is important to mention that the determination of k_r^C at low electron temperatures $T_e \leq 2\,000$ K is generally difficult since it depends strongly on highly excited levels. We have noted in this case, that the more numerous highly excited atomic levels are taken into account, the higher the derived recombination rate is.

Optically thin cases

In optically thin cases, the results obtained for different initial recombining conditions indicate that the three-body recombination rate depends only on the electron temperature

and the electron number density. First, neglecting radiative and dielectronic recombinations, Fig. 7 shows that spontaneous emission increases the value of the recombination rate (denoted, in this case, k_r^{CE}). As expected, at high electron number densities, the recombination rate converges to the value obtained in optically thick cases.

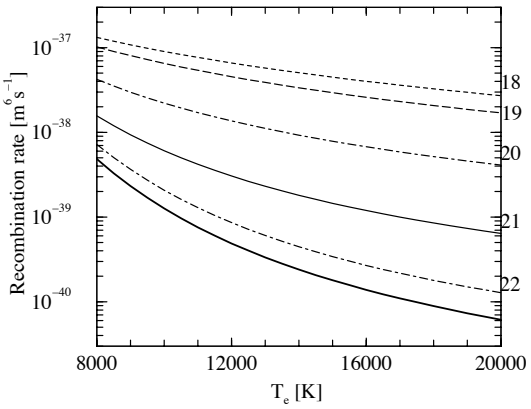

Figure 7: Influence of spontaneous emission on the recombination rate in an optically thin plasma. Numbers at right denote x with $n_e = 10^x$ m^{-3}. The thick solid line corresponds to optically thick cases.

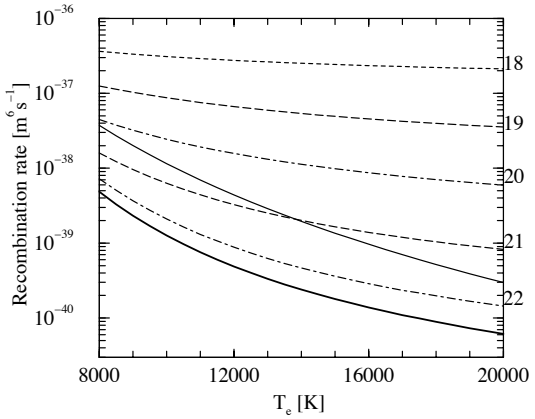

Figure 8: Recombination rate derived in taking into account all elementary processes, in an optically thin plasma. Same notations as Fig. 7. The thin solid line corresponds to the expression proposed by Park (1990).

Conversely, for low electron number densities, k_r^{CE} tends towards an upper limit. If all the elementary processes of section 3.2 are considered, Fig. 8 shows that the influence of radiative and dielectronic recombinations increases as n_e decreases. In this case, the recombination rate has no upper limit at low electron number densities. These results are in qualitative agreement with those obtained earlier by Taylor and Ali (1986). Figure 8 indicates that Park's expression [Eq. (16)], initially proposed for an optically thick case, corresponds to an optically thin plasma where $10^{20} m^{-3} \leq n_e \leq 10^{21} m^{-3}$ and $8000K \leq T_e \leq 20\,000K$.

In order to implement the results of this work in numerical studies on air plasma flows, simple analytical laws are required. In the general Eq. (9), radiative and dielectronic terms can be isolated, then Eq. (13) can be written

$$\frac{dn_e}{dt} = \dot{n_e} = k_i n_e N_a - k_r^{CE} n_e^3 - \alpha^R n_e^2 \tag{17}$$

where k_r^{CE} takes into account all the elementary collisional processes and spontaneous emission (Figure 7), and

$$\alpha^R = \alpha^{RR} + \alpha^{RD} \tag{18}$$

The total effective recombination rate k_r is therefore $k_r^{CE} + \alpha^R / n_e$. This formulation is of great interest since α^{RR} [Eq. (7)] and α^{RD} [Nussbaumer and Storey (1983)] can be

expressed analytically. Then, we fitted k_r^{CE} for different electron number densities to the following expression

$$k_r^{CE} = AT_e^b,\ m^6 s^{-1} \tag{19}$$

for $8000K \leq T_e \leq 20\,000K$. The coefficients A and b are given in Table 2. The discrepancy between the total recombination rate value calculated with the analytical expressions [Eqs. (19) and (18)] and the one determined directly and represented on Fig. 8 remains within a factor of 2.

n_e (m^{-3})	A ($m^6 s^{-1} K^{-b}$)	b
10^{18}	7.27×10^{-31}	-1.73
10^{19}	4.29×10^{-30}	-1.95
10^{20}	2.58×10^{-28}	-2.51
10^{21}	3.19×10^{-25}	-3.43

Table 2: A and b parameters for the effective three-body recombination rate coefficient $k_r^{CE} = AT_e^b,\ m^6 s^{-1}$ for different electron number densities

Comments on the definition of k_r

Following the method described above to determine α^R, one could propose to derive the effective three-body recombination rate coefficient directly from Eq. 9

$$k_r^* = \sum_i \beta_{ci}(T_e) = f(T_e) \tag{20}$$

By definition, this coefficient depends only on T_e and takes into account only direct recombination processes on the atomic levels, and neglects the other processes which link the atomic level populations together. Figure 9 shows that this coefficient k_r^* is slightly higher than $k_{r,max}^{CE}$ which is the maximal value of k_r^{CE}. This coefficient has no physical interest to describe the $O^+ + 2e^- \rightarrow O + e^-$ global recombination process. This result already mentioned by Park (1969) is clearly illustrated here.

3.4.4 Determination of the effective ionization rate coefficient

Optically thick cases

In optically thick cases, the results obtained for different initial ionizing conditions indicate that the effective ionization rate coefficient (denoted k_i^C) depends only on the electron temperature. This can be simply derived from Eq. (14), since in this case, k_r^C depends only on T_e and, the stationary state of the reaction $O^+ + e^- \leftrightarrow O + 2e^-$ corresponds to a Saha equilibrium, therefore $K^{stat} = K^{Saha}(T_e)$. We have fitted the equilibrium constant to the following expression

$$ln(K^{stat}) = \sum_{i=0}^{5} A_i Z^i, \tag{21}$$

where $Z = ln(10^4/T_e)$, for $8000K \leq T_e \leq 20\,000K$. For a Saha equilibrium, the coefficients A_i are given in Table 3. Figure 10 compares the value of k_i^C obtained in our study with three other values often used in high temperature air kinetic schemes, but which accuracy is unknown:

- The effective ionization rate coefficient proposed by Losev et al. (1994) which is derived from the ionization cross section from the ground state measured by Smith et al. (1962).

$$k_{iLosev} = 8.64 \times 10^{-18}\, T_e^{0.68}\, exp\left(\frac{-157980}{T_e}\right)\ \mathrm{m^3 s^{-1}} \tag{22}$$

- The value proposed by Gupta et al. (1990)

$$k_{iGupta} = 59.8\, T_e^{-2.91}\, exp\left(\frac{-158120}{T_e}\right)\ \mathrm{m^3 s^{-1}} \tag{23}$$

- The value proposed by Park (1990)

$$k_{iPark} = 6478.4\, T_e^{-3.78} exp\left(\frac{-158620}{T_e}\right)\ \mathrm{m^3 s^{-1}} \tag{24}$$

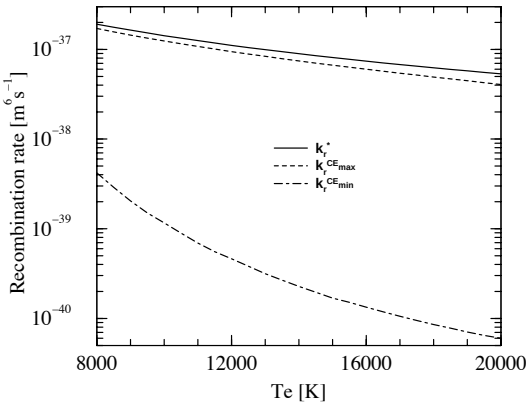

Figure 9: Different definitions of the three-body recombination rate coefficient. k_r^* is the one-way coefficient and $k_{r,min}^{CE}$ and $k_{r,max}^{CE}$ are respectively the minimal and maximal values of k_r^{CE}.

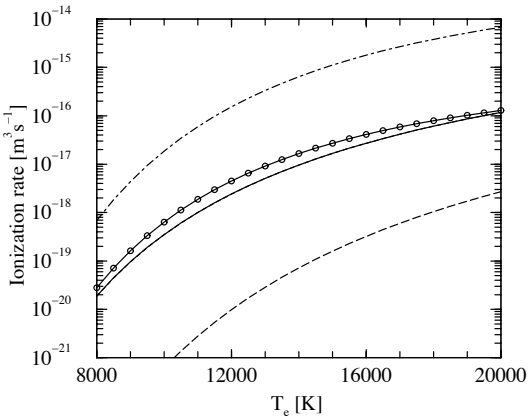

Figure 10: Ionization rate coefficient in optically thick cases. Solid line: our model. Dotted line: Park (1990) Dot-dashed line: Gupta et al. (1990) Dashed line: Losev et al. (1994).

First of all, we note that there are strong discrepancies between the different models. As expected, the value obtained with our model is greater than the one proposed by Losev et al. since the latter takes into account only the ionization process from the ground state. Figure 10 shows that the value proposed by Gupta et al. is overestimated by more than one order of magnitude. In fact, the value of k_i^C obtained with our model turns out to be in close agreement with the one proposed by Park. This result seems to be in disagreement with the discrepancy observed on Fig. 5 between our value of the three-body recombination rate in optically thick cases (k_r^C) and the one proposed by Park (k_{rPark}). In fact, we have noted that the ionization and recombination rate coefficients proposed

N_t (m^{-3})	A_0	A_1	A_2	A_3	A_4	A_5
10^{17}	30.5304	-34.0190	-23.6944	6.18581	-0.916160	-17.5735
10^{18}	32.8715	-33.1659	-22.8399	7.45801	5.02374	-11.8446
10^{19}	35.0493	-31.4172	-24.8850	-0.795804	17.3478	11.0059
10^{20}	36.6971	-27.7121	-6.36738	-49.7549	-187.362	-149.453
10^{21}	38.6205	-35.9083	6.47223	62.7877	-35.6484	-97.7333
10^{22}	41.9019	-45.7554	-37.4442	166.309	443.193	298.333
10^{23}	45.2287	-31.9500	-57.7671	-69.9729	-17.6998	19.8520
K^{Saha}	47.0661	-17.1846	-7.99356	-2.64241	-0.579718	0.182226

Table 3: Parameters in K^{Saha} and in the equilibrium constant K^{stat} for different total particle number densities.

by Park in optically thick cases are not related by the Saha equilibrium constant. That is, $k_{rPark}K^{Saha}$ is on the average 4.7 times greater than k_{iPark}; which is also the average discrepancy observed on Fig. 5 between k_r^C and k_{rPark}.

Optically thin cases

In optically thin cases, radiative processes enhance recombination and then the ionization degree at the stationary state is lower than the one corresponding to the Saha equilibrium. Consequently, $K^{stat} < K^{Saha}(T_e)$, where K^{stat} depends on T_e but also on densities. As explained by Kunc and Soon (1989) the most significative density of the nonequilibrium properties of the stationary state is the total particle density N_t (note that the definition of N_t proposed by these authors is the double of ours) and not the electron number density. As expected, as the density increases, collisional processes become more efficient than radiative ones and, then the equilibrium constant converges toward the Saha equilibrium constant, all the faster since the electron temperature is high. First, neglecting radiative and dielectronic recombination processes, the equilibrium constant tends toward a lower limit for low values of N_t. When radiative and dielectronic recombination processes are taken into account, this lower limit disappears. As Soon and Kunc (1990) considered more accurately the reabsorption of the emitted radiation, a direct comparison with their results at the stationary state is impossible. However, a qualitative agreement is observed. Finally, to implement our results in flow codes, we have fitted K^{stat} for different values of N_t to the expression of Eq. (21) for $8000K \leq T_e \leq 20\,000K$. The coefficients A_i are given in Table 3. The discrepancy between the ionization rate coefficient value calculated with the analytical expression [Eq. (21)] and the one determined directly remains within a factor of 2 (Bourdon et al. (1998)).

3.4.5 Study of the quasi-steady-state relaxation time

In the previous sections, we have put forward that effective three-body recombination and ionization rate coefficients exist only when the system is in a quasi-steady-state. Therefore, before implementing these rate coefficients in flow codes, one has to check the validity of the QSS hypothesis [Eq. (11)]. The time-dependent approach used in this work allows us to determine the relaxation time necessary to reach a quasi-steady-state, starting at

$t = 0s$ from a given initial condition.

Optically thick cases

For optically thick cases, the results obtained for different initial conditions (either ionizing or recombining) indicate that the quasi-steady-state relaxation time (denoted τ^C_{QSS}) depends only on the electron temperature and electron number density but not on the initial distribution on the atomic levels. Figure 11 shows that τ^C_{QSS} depends only weakly on T_e but increases as n_e decreases. For $n_e = 10^{19}m^{-3}$, the relaxation time derived in using Gryzinski's cross sections for all levels is also represented. The latter is one order magnitude shorter than the one obtained with our model. It is interesting to note that relaxation times obtained in oxygen are very close to those calculated in nitrogen (Bourdon and Vervisch (1996)). Finally, Fig. 11 shows that the effective ionization and recombination rate coefficients determined in this work are adapted to study optically thick plasma flows, where the characteristic flow time is about 10^{-6} s, only if $n_e \geq 10^{20}m^{-3}$. For lower electron number densities or shorter flow times, it is necessary to consider one conservation equation for each atomic level i of the oxygen atom.

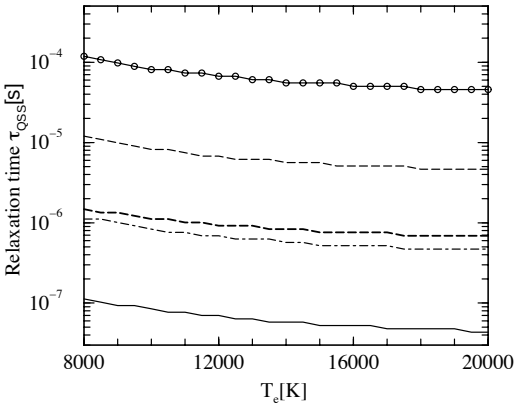

Figure 11: Relaxation time in optically thick cases. Thin solid line with open circles: $n_e = 10^{18}\mathrm{m}^{-3}$. Thin dashed line: $n_e = 10^{19}\mathrm{m}^{-3}$. Thin dot-dashed line: $n_e = 10^{20}\mathrm{m}^{-3}$. Thin solid line: $n_e = 10^{21}\mathrm{m}^{-3}$. The thick dashed line represents the results obtained for $n_e = 10^{19}\mathrm{m}^{-3}$ in using the cross sections derived by Gryzinski (1965).

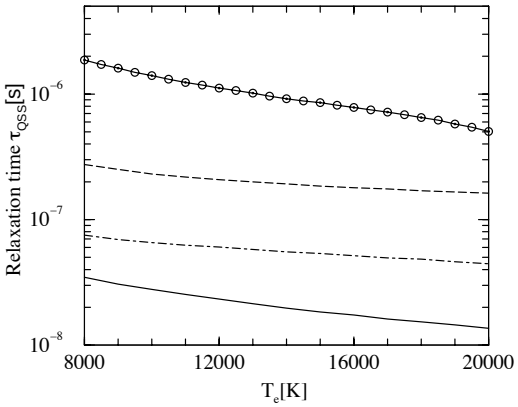

Figure 12: Relaxation time in optically thin cases with at t =0s, $b_i = N_i/N_i^*$ =1, for a given electron number density. Solid line with open circles: $n_e = 10^{18}\mathrm{m}^{-3}$. Dashed line: $n_e = 10^{19}\mathrm{m}^{-3}$. Dot-dashed line: $n_e = 10^{20}\mathrm{m}^{-3}$. Solid line: $n_e = 10^{21}\mathrm{m}^{-3}$.

Optically thin cases

In an optically thin plasma, the relaxation time depends on densities and T_e but also on the initial distribution on atomic levels. Therefore, it is more difficult to derive general results. However, we have noted that for initial recombining conditions with at t =0 s $b_i = N_i/N_i^* \leq 1$ (where N_i^* is the Saha density of level i) for a given electron number

density, the QSS relaxation time depends only on n_e and T_e. In these cases, Fig. 12 shows that the QSS relaxation time depends weakly on T_e and increases as n_e decreases. In comparison to an optically thick case, we note that relaxation times are on the average one order of magnitude shorter.

3.5 Conclusions

In this work, we have shown how to use a detailed collisional radiative model to determine the effective ionization and three-body recombination rate coefficients of oxygen in a plasma where $10^{18}m^{-3} \leq n_e \leq 10^{21}m^{-3}$ and $8000K \leq T_e \leq 20\,000K$. The time-dependent approach used in this work has clearly put forward the necessity that the system be in a quasi-steady state to derive meaningful rate coefficients. This has led us to study more precisely the relaxation time τ_{QSS} necessary to reach a quasi-steady-state.
In this work, the treatment of radiation has been reduced to optically thin or thick cases. It would be interesting to take into account a more accurate modeling of radiation escape factors in order to study more precisely the influence of the reabsorption of radiation. However, this effect will not change the general characteristics of the results obtained in this paper.

4 Collisional-radiative model for air

The previous section has shown that a temporal description of the chemistry of a plasma is the most relevant approach to understand its behavior by a fundamental point of view: this approach is the only one allowing to check the conditions for using a ionization or recombination rate coefficient. As a result, we have chosen to reproduce such a study but for a more complicated medium where molecules play a role in order to see if a quasi steady-state still exists. Moreover, this study is also motivated by our main objective: the more realistic calculation of the interaction between a plasma formed during an atmospheric re-entry of a spacecraft and its thermal shield. In that case, the flow is indeed very rapid: as illustrated in the following, the chemistry is therefore time-dependent in Lagrangian description.

4.1 Atomic and molecular model

In this work, air considered is a mixture of heated nitrogen and oxygen and their products: argon as other gas traces are neglected. Due to the wide range of temperatures and pressure studied, we take into account N_2, O_2, N, O, NO, N_2^+, O_2^+, N^+, O^+, NO^+, O_2^-, O^- and electrons. For each species, we consider electronic excited states except for N^+, O^+, O^- and O_2^- as shown in Table 4. The energetic data are due to Herzberg (1950), Capitelli et al. (2000a) and Park (1990). 46 levels for N and the previous 40 levels for O are taken into account in order to calculate correctly the recombination of N^+ and O^+ respectively by three-body processes and in order to estimate thoroughly the net population density of the metastable states $^2D^0$ and $^2P^0$ for nitrogen and ^1D and ^1S for oxygen resulting from the electron and heavy particles induced processes. In addition, that provides the calculation of the excited population densities which are the source of the radiative signature of the medium. The levels considered for N are those already mentioned by Bourdon

Type	Species	State
Molecules	N_2	$X^1\Sigma_g^+$, $A^3\Sigma_u^+$, $B^3\Pi_g$, $C^3\Pi_u$
	O_2	$X^3\Sigma_g^-$, $a^1\Delta_g$, $b^1\Sigma_g^+$, $A^3\Sigma_u^+$, $B^3\Sigma_u^-$
	NO	$X^2\Pi$, $A^2\Sigma^+$, $B^2\Pi$, $C^2\Pi$, $B'^2\Delta$
Molecular ions	N_2^+	$X^2\Sigma_g^+$, $A^2\Pi_u$, $B^2\Sigma_u^+$, $C^2\Sigma_u^+$
	O_2^+	$X^2\Pi_g$, $a^4\Pi_u$, $A^2\Pi_u$, $b^4\Sigma_g^-$
	NO^+	$X^1\Sigma^+_{(v=0\rightarrow 14)}$, $a^3\Sigma^+$, $b^3\Pi$, $b'^3\Sigma^-$, $A^1\Pi$
	O_2^-	$X^2\Pi_g$
Atoms	N	$^4S^0$,... (46 levels)
	O	^3P,... (40 levels)
Atomic ions	N^+	^3P
	O^+	$^4S^0$
	O^-	^2P

Table 4: Species taken into account in the present CR model.

and Vervisch (1996).
Moreover, since the rate coefficient for dissociative recombination of NO^+ has been calculated for each excited vibrational level between $v = 0$ and $v = 14$ (Motapon et al. (2006)), the vibrational excitation of this ion is explicitly considered contrary to the case of the other molecular species for which the assumption of equilibrium at T_e is done.
All in all, this atomic and molecular model represents 131 different levels and their coupling in the frame of the present physical situation is ensured by the following elementary processes.

4.2 Elementary processes

4.2.1 Radiative processes

We take into account 45 spontaneous emission lines for N and 24 for O for which Einstein's probability is higher than $5\times10^3\ s^{-1}$ for N and $3\times10^5\ s^{-1}$ pour O. In addition, we account for the radiative and dielectronic recombinations. The calculations and data for all these radiative processes are similar to those of the previous section.
The possible re-absorption of the radiations is estimated by the following escape factor:

$$T(l) = \int_0^1 \frac{e^{-k_0\, l\, x} dx}{\sqrt{-\pi \ln x}} \tag{25}$$

derived from the work of Holstein (1947) with a typical plasma thickness equal to that of the boundary layer (typically of the order of $l = 1\,cm$) and assuming a Doppler broadening for which k_0 is the absorption coefficient by unit length at the centerline. Any pressure broadening is assumed negligible, the maximum pressure level being atmospheric. In the

same way, the role of charged particles is not considered since the electron density n_e is sufficiently weak.
Some of the states of the species mentioned in Table 4 radiate importantly. The β ($B^2\Pi \rightarrow X^2\Pi$) and γ ($A^2\Sigma^+ \rightarrow X^2\Pi$) systems of NO as well as the first positive ($B^3\Pi_g \rightarrow A^3\Sigma_u^+$) and the second positive ($C^3\Pi_u \rightarrow B^3\Pi_g$) systems of N_2 and the first negative system ($B^2\Sigma_u^+ \rightarrow X^2\Sigma_g^+$) of N_2^+ have been considered. Since a vibrational equilibrium is assumed for these species at the electron temperature T_e, the equivalent transition probability for the latter systems is calculated by:

$$A = \frac{\sum_{v'}(\sum_{v"} A_{v'v"})e^{-\frac{G(v')}{k_B T_e}}}{\sum_{v'} e^{-\frac{G(v')}{k_B T_e}}} \tag{26}$$

where $G(v')$ is the vibrational energy, $A_{v'v"}$ the vibrational transition probability and k_B the Boltzmann constant. Using the data calculated by Laux and Kruger (1992), we have fitted each value of A by:

$$A = \sum_{i=0}^{3} a_i \, T_e^i \tag{27}$$

whose coefficients a_i are calculated for $2000\,K \leq T_e \leq 12000\,K$ and may be obtained on demand.

4.2.2 Collisional processes

Electron induced processes
When available, the cross sections are chosen in accordance with the more recent experimental data. Since the Maxwell equilibrium assumption is done for most of the species, the cross sections have been integrated and the rate coefficient obtained finally fitted under the form:

$$k_{i\rightarrow j}(T_e) = A\,T_e^{-\alpha}\,e^{-\theta/T_e} \tag{28}$$

In Table 5 are summed up the parameters A, α and θ hence calculated for $2000\,K \leq T_e \leq 10000\,K$. The rate coefficient for the excitation of molecular species under electron impact has been calculated recently by Teulet et al. (1999) under the form of Eq.(28) and are used in the present work.
There are few data concerning the ionization of N and O, especially for the highly excited states. For the ground state, we have used for both atoms the cross sections reviewed by Tawara and Kato (1999). Conversely, we have preferred the cross sections obtained by Kim and Desclaux (2002) for metastable nitrogen and assumed that the cross section for metastable oxygen has the same form when the shift due to the different threshold is taken into account. The derived rate coefficients expressed by Eq.(28) use the parameters mentioned in Table 5. For higher excited levels, the classical cross sections of Drawin are used considering that each atom has only one optical electron.
The data related to the ionization of molecules are taken from the work of Teulet et al. (1999) as those concerning the dissociation.

Heavy particles induced processes
The excitation of atoms due to atom collisions has been discussed by Capitelli et al.

i	j	A	α	θ	Ref.
$N(^4S^0)$	$N(^2D)$	1.720×10^{-15}	-0.280	28250	Berrington et al. (1975)
$N(^4S^0)$	$N(^2P)$	4.004×10^{-16}	-0.324	42860	Berrington et al. (1975)
$O(^3P)$	$O(^1D)$	1.374×10^{-17}	-0.566	24600	Itikawa et al. (1990)
$O(^3P)$	$O(^1S)$	9.352×10^{-19}	-0.620	50110	Itikawa et al. (1990)
$N(^4S^0)$	$N^+(^3P)$	8.583×10^{-16}	-0.276	166870	Tawara and Kato (1999)
$N(^2D)$	$N^+(^3P)$	7.732×10^{-18}	-0.711	139900	Kim and Desclaux (2002)
$N(^2P)$	$N^+(^3P)$	1.026×10^{-17}	-0.677	126310	Kim and Desclaux (2002)
$O(^3P)$	$O^+(^4S^0)$	5.393×10^{-18}	-0.750	158330	Tawara and Kato (1999)
$O(^1D)$	$O^+(^4S^0)$	8.571×10^{-18}	-0.695	134190	Kim and Desclaux (2002)
$O(^1S)$	$O^+(^4S^0)$	1.397×10^{-17}	-0.647	108800	Kim and Desclaux (2002)

Table 5: Parameters A, α and θ for the calculation of the rate coefficient (in $m^3\,s^{-1}$) given by Eq.(28) for the transition $i \rightarrow j$ induced by electron collision. θ is expressed in K.

(2000a) between the ground and metastable levels. We have consequently considered all these data in our CR model. On the other hand, we have adopted a linear form for the cross section σ_{ij}^A with the relative kinetic energy ϵ of the colliding particles for excitation from the ground or the metastable states towards highly excited levels:

$$\sigma_{ij}^{A-A}(\epsilon) = \beta_{ij}^{A-A}(\epsilon - E_{ji}) \tag{29}$$

where E_{ji} is the threshold. Since the parameter β_{ij}^{A-A} weakly depends on the mass of the colliding particles (Drawin and Emard (1973)), we have assumed that the cross section can be derived from the case of argon (Bultel et al. (2002)) taking the mean value $\beta_{ij}^{A-A} = 3.4 \times 10^{-25}\,m^2\,eV^{-1}$. For excitation between higher excited levels, we have considered, as in the case of argon, that Eq.(29) is applicable with:

$$\beta_{ij}^{A-A} = 8.69 \times 10^{-22} E_{ji}^{-2.26} \quad m^2\,eV^{-1} \tag{30}$$

The cross section for excitation of atoms under molecule impact behaves approximately as (Lotz (1968)):

$$\sigma_{ij}^{A-M}(\epsilon) = \sigma_0 \frac{\ln(\epsilon/E_{ji})}{\epsilon/E_{ji}} \tag{31}$$

where $\sigma_0 \simeq 10^{-20}\,m^2$. This form has been adopted.
Equation (31) is also assumed to condition the excitation of any molecular species under atom or molecule impact except in the case when experimental data exist. We have then preferred the rate coefficients compiled by Teulet et al. (2001), Capitelli et al. (2000a) and Kossyi et al. (1992).
From these sets of rate coefficients, we have also extracted and used those related to charge transfer (with possible reassociation of atoms to form a molecule), reassociation, excitation transfer, ionization, dissociation, neutralization of O^- and O_2^- and attachment and detachment. Due to the pressure levels involved in our CR model, we have also taken into account the previous processes occurring when a third particle interacts.

Two reactions are known to highly influence the distribution of nitrogen and oxygen between atomic and molecular systems. These reactions called Zeldovich's reactions are:

$$O_2 + N \overset{(1)}{\rightarrow} NO + O \tag{32a}$$

$$N_2 + O \overset{(2)}{\rightarrow} NO + N \tag{32b}$$

Recently, Bose and Candler have up-dated their rate coefficient using a quasiclassical trajectory method performed starting from an *ab initio* potential surfaces calculation. They have obtained:

$$k_1(T_A) = 4.14 \times 10^{-21}\, T_A^{1.179}\, e^{-4000.5/T_A} \quad m^3\, s^{-1} \tag{33}$$

for the process (32a) (Bose and Candler (1997)) and:

$$k_2(T_A) = 9.45 \times 10^{-18}\, T_A^{0.420}\, e^{-42940/T_A} \quad m^3\, s^{-1} \tag{34}$$

for the process (32b) (Bose and Candler (1996)). The rate coefficients (33) and (34) are used in our work.
The processes (32a) and (32b) can contribute to the destruction of O_2 and N_2 and formation of NO. Of course, the direct dissociation and the reverse process by heavy particles impact have to be taken into account. The rate coefficients used are due to Losev and Shatalov (1990) who have assumed the vibrational mode in equilibrium with the electrons at T_e. We refer to their paper for more details.

4.2.3 Dissociative recombination of N_2^+, O_2^+ and NO^+

The dissociative recombination (DR) of the molecular ions, which is the subject of a very intensive work (Guberman (2003)), is well-known to play a very important role in the case of recombining plasmas even at low pressure (Bultel et al. (2002)). In addition, the inverse process, the associative ionization, allows in much cases the formation of the first electrons in shock tube (Drawin and Emard (1973)) as well as for the re-entries problems and consequently explain the ionizing situations. In our case, since N_2^+, O_2^+ and NO^+ are present in the plasmas described here, dissociative recombination has to be considered.

Dissociative recombination of N_2^+
The dissociative recombination of N_2^+ has been investigated in the CRYRING storage ring by Peterson et al. (1998) over a wide range for electron energy ($10\,meV < \epsilon < 30\,eV$). They have shown that its rate coefficient is weakly dependent on the vibrational state v of the molecular ion and can be set equal to:

$$\alpha_{N_2^+} = 1.75 \times 10^{-13} \left(\frac{T_e}{300}\right)^{-0.30} m^3 s^{-1} \tag{35}$$

In addition, they have obtained the branching fractions $\gamma_i(N_2^+)$ for $v = 0$ at $0\,eV$ collision energy for the following products formation:

$$N_2^+ + e^- \overset{\gamma_1(N_2^+)}{\longrightarrow} N(^4S^0) + N(^2D) \tag{36a}$$

$$N_2^+ + e^- \xrightarrow{\gamma_2(N_2^+)} N(^4S^0) + N(^2P) \tag{36b}$$

$$N_2^+ + e^- \xrightarrow{\gamma_3(N_2^+)} N(^2D) + N(^2D) \tag{36c}$$

with $\gamma_1(N_2^+) = 0.37$, $\gamma_2(N_2^+) = 0.11$ and $\gamma_3(N_2^+) = 0.52$. The collision energy range of their experiment includes our own (derived from the electron temperature T_e levels considered in this work). Moreover, although the rate coefficient found weakly depends on the vibrational excitation of the molecular ion, the vibrational temperature of N_2^+ in the experiment of Peterson *et al.* corresponds well to the case of the plasmas considered in this paper ($T_v = T_e \simeq 6000\,K$ on average). For all these reasons, their results have been integrated in our calculations.

Dissociative recombination of O_2^+

The dissociative recombination of O_2^+ has been investigated in the same heavy ion storage ring by Peverall et al. (2001) but only on the collision energy range $1\,meV < \epsilon < 3\,eV$ due to the collapse of the cross section for higher energies. The rate coefficient derived is:

$$\alpha_{O_2^+} = 2.4 \times 10^{-13} \left(\frac{T_e}{300}\right)^{-0.70} m^3 s^{-1} \tag{37}$$

where the molecular ion is in the vibrational fundamental state. The branching fractions ascribed to the processes:

$$O_2^+ + e^- \xrightarrow{\gamma_1(O_2^+)} O(^3P) + O(^3P) \tag{38a}$$

$$O_2^+ + e^- \xrightarrow{\gamma_2(O_2^+)} O(^3P) + O(^1D) \tag{38b}$$

$$O_2^+ + e^- \xrightarrow{\gamma_3(O_2^+)} O(^1D) + O(^1D) \tag{38c}$$

are respectively equal to 0.20, 0.40 and 0.40. Although the branching fraction for the process:

$$O_2^+ + e^- \rightarrow O(^1D) + O(^1S) \tag{39}$$

is not equal to 0, its order of magnitude and the fact that it becomes almost 0 for collision energies between 10 and $40\,meV$ by increasing up to 0.06 for $\epsilon = 300\,meV$ led us to consider finally that this channel is closed and that the dissociative recombination for O_2^+ occurs by the processes (38a), (38b) and (38c) only. Founding no more information in the literature about a possible influence of the vibrational excitation of O_2^+ on the dissociative recombination rate coefficient, we have assumed no influence and consequently adopted Eq.(37) and the previous branching fractions.

Dissociative recombination of NO^+

The case of NO^+ has to be particularly discussed: as we will see in the subsequent part of this paper, this molecular ion plays a very important role. As in the previous case of N_2^+ and O_2^+, three factors condition the discussion: the vibrational excitation of the molecular ion, the collision energy range and the branching fractions. Early works were devoted to the experimental determination of the rate coefficient in room temperature conditions for kinetics in post-discharge purposes (Gunton and Shaw (1965)) (Weller and

Biondi (1968)): NO^+ is then on its vibrational ground state and the collision energy range is very weak. Other determinations of the rate coefficient were also performed for larger collision energy ranges (Huang et al. (1975)). With the development of the hypersonic flights, experiments were done also in shock-tubes where the rate coefficient was determined (Dunn and Lordi (1969)) or calculated (Hansen (1968)): the vibrational excitation of the molecular ion was higher consequently as well as the collision energy range ($T_e < 6000\,K$ in order of magnitude). Several theoretical treatments have been applied to explain the experimental values. We mention the work of Bardsley (1983) and those of Sun and Nakamura (1990) whose results, obtained with different methods, reveal that the cross section for $v > 0$ can be higher by one order of magnitude than for $v = 0$ when $\epsilon > 1\,eV$. Since a calculation of the Maxwell rate coefficient needs the value of the cross section up to $\epsilon = 10\,eV$ for $T_e = 1\,eV$, the vibrational excitation of NO^+ may have an influence on the global dissociative recombination. In order to use an accurate value for the cross section on the previous collision energy range and in particular in order to access to the role of the vibrational excitation, we have used the results of the extensive calculations using the Multichannel Quantum Defect Theory (MQDT) developed by Motapon et al. (2006) resulting, among other data, in the cross section $\sigma_{DR}(\epsilon, v)$ of the dissociative recombination:

$$NO^+(X^1\Sigma^+, v) + e^-(\epsilon) \overset{\sigma_{DR}(\epsilon,v)}{\longrightarrow} N^* + O^* \tag{40}$$

This kind of reaction can occur in fact according to two channels.

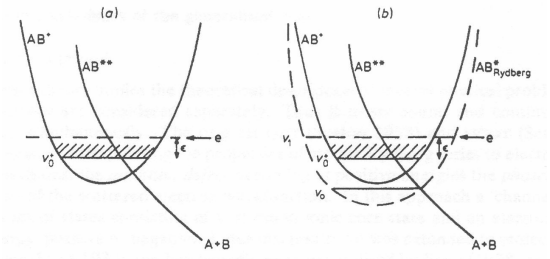

Figure 13: Schematic view of the two channels allowing the dissociative recombination of a molecular ion AB with electron. Left: the direct process, right: the indirect process. The electron energy is ϵ. AB^{**} is a dissociative potential curve of the molecule AB.

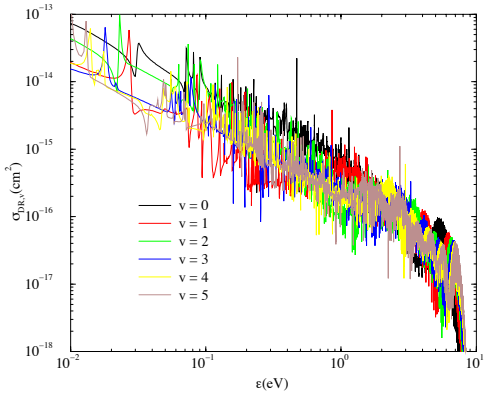

Figure 14: Cross section $\sigma_{DR}(\epsilon, v)$ for dissociative recombination of NO^+ with electron for different vibrational excitation of the ion ($0 \leq v \leq 5$).

First, the DR can be due to a direct process: it leads to the formation of a doubly excited state of NO, denoted NO^{**}, which dissociate spontaneously afterwards by producing separated N and O atoms possibly electronically excited (see Fig.13). The estimation of the cross section needs consequently an accurate knowledge of the potential curves for these states. The higher the energy for the electron, the more numerous the potential

curves. Second, the DR can also occur through an indirect process: this process leads to the formation of a Rydberg level of NO associated with a vibrationnally excited state of NO^+ which is predissociated by the NO^{**} state. In this case, the Rydberg states being numerous by definition, the calculation of the contribution of the indirect channel to the cross section needs a great amount of molecular data.
Both channels need finally numerous data and one of the main issues to be addressed is the thorough determination of the potential curves related to the states involved. After such a determination, several methods can be applied in order to calculate the cross section. One of the most efficient one at the present time is based on the Multi-Channel Quantum Defect Theory. Its approach is based on a description of molecular states in which only part of the electronic hamiltonian is diagonalized, within subspaces of electronic states with similar nature. We refer to the paper of Motapon et al. (2006) for more details.
We can observe on Fig.14 the behavior of the cross section resulting from the energy of the colliding electron and the vibrational excitation of the molecular ion calculated by the MQDT approach. The influence of the great number of states is obvious: the cross section presents much oscillations which correspond to resonances when the energy of the electron is accorded with the difference between two particular states involved. In addition, the global behavior does not follow a ϵ^{-1} law contrary to that usually assumed. In particular, when the energy of electron exceeds $7\,eV$, the cross section collapse.
The Maxwellian rate coefficient of the DR is derived from the calculation of the cross section. Each rate coefficient is finally fitted under the general modified Arrhenius law (28). We can find in Table 6 the parameters A, α and θ for each value of the vibrational quantum number v between 0 and 5. The usual form adopted for the cross section leads

v	A	α	θ
0	8.486×10^{-11}	0.793	859.99
1	3.958×10^{-14}	0.076	−661.83
2	1.664×10^{-11}	0.704	−39.13
3	6.335×10^{-13}	0.383	−282.98
4	2.970×10^{-13}	0.311	−632.21
5	2.666×10^{-13}	0.297	−472.45

Table 6: Parameters A, α and θ for the calculation of the rate coefficient (in $m^3\,s^{-1}$) given by Eq.(28) for the dissociative recombination of $NO^+(X^1\Sigma, v)$ with electrons used in this work Motapon et al. (2006). θ is expressed in K.

to a rate coefficient following a $T^{-0.5}$ law. The characteristic temperature θ being rather small, the temperature dependence is mainly due to α. Table 6 shows that the rate coefficient is relatively different from a value of the vibrational quantum number v to another with a form far from a $T^{-0.5}$ law: as a result, the usual temperature dependence is consequently not realistic and too simplistic. Assuming an equilibrium between the vibration of NO^+ and electrons, these values lead to that of the global rate coefficient for the dissociative recombination:

$$k_{DR}(T) = 1.658 \times 10^{-10}\, T^{-0.933}\, e^{-377.68/T} \qquad m^3 s^{-1} \tag{41}$$

where the main temperature dependence is due to the $T^{-0.933}$ term. This form reveals that the common law adopted for the DR is erroneous. This conclusion can be made also in the case of N_2^+ and O_2^+ whose rate coefficient presents a temperature dependence according to a $T^{-0.3}$ and $T^{-0.7}$ law respectively as experimentally determined.
The more realistic view of the process (40) needs to know the excitation of nitrogen and oxygen atoms after the recombination. As far as we know, only three works were devoted to this difficult issue. The earliest one, due to Kley et al. (1977) and performed by photoionization of buffered nitric oxide by a flash lamp, reported that only two channels are open:

$$NO^+(X^1\Sigma^+) + e^- \xrightarrow{\gamma_1} N(^4S^0) + O(^3P) \tag{42}$$

and

$$NO^+(X^1\Sigma^+) + e^- \xrightarrow{\gamma_2} N(^2D) + O(^3P) \tag{43}$$

with $\gamma_1 = 0.24 \pm 0.06$ and $\gamma_2 = 0.76 \pm 0.06$. It is important to note that these results have been obtained with a Maxwellian distribution for the kinetic energy ϵ of colliding particles. Controlling ϵ, Vejby-Christensen et al. (1998) have more recently determined the branching fractions in the ASTRID ion storage ring for a collision energy $\epsilon = 0$, 0.75 and $1.35\,eV$. They confirm in part the results of Kley et al. but with γ_1 rather equal to 0.15 ± 0.06 for $\epsilon = 0\,eV$ and not well identified for $\epsilon = 0.75$ and $1.35\,eV$. For these two collision energies, they concluded only that the process (43) represents at least 65% of the dissociative recombination events. Finally, Hellberg et al. (2003) have investigated the dissociative recombination of the $X^1\Sigma^+$ and $a^3\Sigma^+$ states in the CRYRING storage ring and succeeded for the ground electronic state to measure the branching fractions for $\epsilon = 0, 1.25$ and $5.6\,eV$. Increasing the collision energy leads to a multiplication of the branching. Table 7 illustrates their results compared to those of Kley et al. and Vejby-Christensen et al. Since our CR model is elaborated to work over a wide range of temperature, each one corresponding to a Maxwell distribution of the collision energy, the temperature dependent branching fraction $\gamma_i(T_e)$ for each i channel has to be determined. The values finally retained in our work result from the following considerations and are based on the data of Hellberg *et al.* due to their best precision. When the collision energy is insufficient, the branching fraction is put equal 0. This is the case at different energies of all the channels involved except those producing $N(^4S^0) + O(^3P)$ and $N(^2D) + O(^3P)$ for which the processes are exothermic. Since the branching fraction for the production of $N(^4S^0) + O(^1D)$ is always 0 considering the uncertainty range, we have assumed that this channel is systematically closed.
Moreover, the branching fraction is assumed independent of the collision energy when the collision energy is greater than the threshold (which is equal to 0.81, 1.59, 2.78, 3.81 and $5.0\,eV$ for the processes 3 up to 7 respectively). For the channels (42) and (43), the values adopted are chosen over the uncertainty range in order that the sum of branching fractions be equal to unity. As a result, the branching fractions obtained according to the energy ranges are summed up in Table 8. The temperature dependent branching fraction $\gamma_i(T_e)$ for the i-process is finally obtained by:

$$\gamma_i(T_e) = \frac{\displaystyle\int_0^{+\infty} \gamma_i(\epsilon)\, x\, e^{-x}\, \sigma_{DR}(x)\, dx}{\displaystyle\int_0^{+\infty} x\, e^{-x}\, \sigma_{DR}(x)\, dx} \tag{44}$$

Ref.	Process	Process i	Branching fraction γ_i
K.	$NO^+(\bar{v}=1.5) + e^-(\bar{\epsilon}=0.34\,eV) \longrightarrow N(^4S^0) + O(^3P)$	1	0.24 ± 0.06
K.	$NO^+(\bar{v}=1.5) + e^-(\bar{\epsilon}=0.34\,eV) \longrightarrow N(^2D) + O(^3P)$	2	0.76 ± 0.06
V.-C.	$NO^+(0) + e^-(0\,eV) \longrightarrow N(^4S^0) + O(^3P)$	1	0.15 ± 0.06
V.-C.	$NO^+(0) + e^-(0\,eV) \longrightarrow N(^2D) + O(^3P)$	2	0.85 ± 0.06
V.-C.	$NO^+(0) + e^-(0.75, 1.35\,eV) \longrightarrow N(^2D) + O(^3P)$	2	> 0.65
H.	$NO^+(0) + e^-(0\,eV) \longrightarrow N(^4S^0) + O(^3P)$	1	0.05 ± 0.02
H.	$NO^+(0) + e^-(0\,eV) \longrightarrow N(^2D) + O(^3P)$	2	0.95 ± 0.02
H.	$NO^+(0) + e^-(1.25\,eV) \longrightarrow N(^4S^0) + O(^3P)$	1	0.10 ± 0.06
H.	$NO^+(0) + e^-(1.25\,eV) \longrightarrow N(^2D) + O(^3P)$	2	0.70 ± 0.20
H.	$NO^+(0) + e^-(1.25\,eV) \longrightarrow N(^4S^0) + O(^1D)$	-	0.10 ± 0.10
H.	$NO^+(0) + e^-(1.25\,eV) \longrightarrow N(^2P) + O(^3P)$	3	0.10 ± 0.07
H.	$NO^+(0) + e^-(5.6\,eV) \longrightarrow N(^4S^0) + O(^3P)$	1	0.03 ± 0.02
H.	$NO^+(0) + e^-(5.6\,eV) \longrightarrow N(^2D) + O(^3P)$	2	0.15 ± 0.05
H.	$NO^+(0) + e^-(5.6\,eV) \longrightarrow N(^2P) + O(^3P)$	3	0.11 ± 0.05
H.	$NO^+(0) + e^-(5.6\,eV) \longrightarrow N(^2D) + O(^1D)$	4	0.31 ± 0.05
H.	$NO^+(0) + e^-(5.6\,eV) \longrightarrow N(^2P) + O(^1D)$	5	0.21 ± 0.05
H.	$NO^+(0) + e^-(5.6\,eV) \longrightarrow N(^2D) + O(^1S)$	6	0.09 ± 0.05
H.	$NO^+(0) + e^-(5.6\,eV) \longrightarrow N(^2P) + O(^1S)$	7	0.10 ± 0.05

Table 7: Comparison between experimental information available on the branching fractions of the dissociative recombination of $NO^+(X^1\Sigma^+, v)$. The value $\bar{v}=1.5$ means that NO^+ is weakly vibrationally excited. The value $\bar{\epsilon}=0.34\,eV$ means that the collision energy is distributed according to a Maxwell distribution. $K.$, $V.-C.$ and $H.$ mean Kley et al. (1977), Vejby-Christensen et al. (1998) and Hellberg et al. (2003) respectively.

Energy range (eV)	γ_1	γ_2	γ_3	γ_4	γ_5	γ_6	γ_7
$[0; 0.81[$	0.07	0.93	0.00	0.00	0.00	0.00	0.00
$[0.81; 1.59[$	0.15	0.75	0.10	0.00	0.00	0.00	0.00
$[1.59; 2.78[$	0.03	0.55	0.11	0.31	0.00	0.00	0.00
$[2.78; 3.81[$	0.03	0.34	0.11	0.31	0.21	0.00	0.00
$[3.81; 5[$	0.03	0.25	0.11	0.31	0.21	0.09	0.00
$[5; 10[$	0.03	0.15	0.11	0.31	0.21	0.09	0.10

Table 8: Branching fractions $\gamma_i(\epsilon)$ for i-process (see Table 7) adopted for the calculation of the temperature dependent branching fractions of the dissociative recombination of $NO^+(X^1\Sigma^+, 0)$ with electrons.

where $x = \epsilon/(k_B T_e)$ and σ_{DR} the dissociative recombination cross section. Figure 15 shows the branching fractions calculated with the help of the cross section determined by the MQDT approach. In the following, we have assumed that the branching fractions behave for $v > 0$ like for $v = 0$.

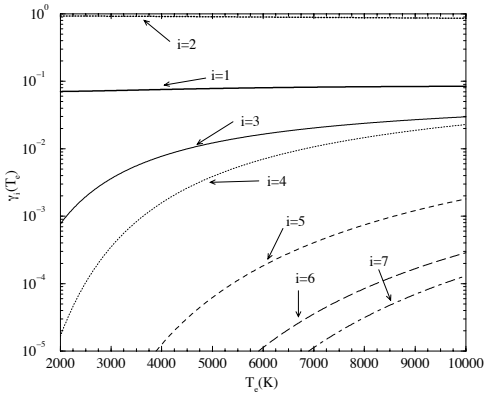

Figure 15: Temperature dependent branching fractions obtained with our calculated cross section for the dissociative recombination of $NO^+(X^1\Sigma^+, 0)$ for the different channels investigated by Hellberg et al. (see Table 7 and 8).

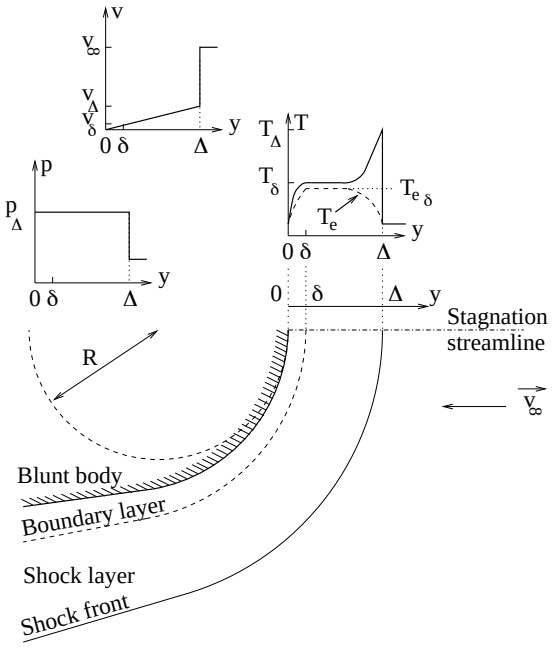

Figure 16: Considered situations of reentry displaying the pressure, velocity and temperatures profiles along the stagnation streamline.

The fact that the rate coefficient depends strongly upon v has led us to develop a state to state kinetics for NO^+.

4.2.4 Vibrational processes

Due to the lack of experimental or theoretical investigations allowing the determination of the cross section of vibration-vibration (VV) and vibration-translation (VT) processes involving NO^+, we assume that this ion behave like N_2 for which Armenise et al. (1996) and Billing and Fisher (1979) have produced very useful data. Conversely, the case of vibration-electron (VE) processes like:

$$NO^+(X^1\Sigma^+, v_i) + e^- \rightarrow NO^+(X^1\Sigma^+, v_f) + e^- \tag{45}$$

corresponding to inelastic collisions when $v_f > v_i$ and to super-elastic collisions in the reverse case can be treated by the MQDT approach. The cross sections have been determined and the Maxwellian rate coefficients derived. These rate coefficients have been fitted under the form (28).

4.3 Results

4.3.1 Ionization situation

Although the CR model elaborated with the help of the previous data can work up to the atmospheric pressure, we will discuss in the following some typical re-entry situations only displayed for instance by Fig.16 where the pressure is clearly lower.
We have chosen to develop our study from a temporal point of view as already developed in the section devoted to the elaboration of CR model for atoms. This choice will be justified later.
The general balance equation for a species X on one of its excited levels i can be written indeed by displaying the hydrodynamic derivative D/Dt relevant under a Lagrangian description of the flow:

$$\frac{D[X(i)]}{Dt} + [X(i)]\,\vec{\nabla}\,\vec{v} = -\vec{\nabla}\,\vec{J}_{X_i} + \left[\frac{\partial[X(i)]}{\partial t}\right]_{CR} \tag{46}$$

This form is particularly well adapted to estimate the importance of each contribution in the balance: comparing their characteristic time scale is enough. In order to estimate correctly the one related to the chemical source $[\partial[X(i)]/\partial t]_{CR}$, we assume that the characteristic time scale for the fluid expansion of contraction taken into account in the balance equation by the term $[X(i)]\,\vec{\nabla}\,\vec{v}$ and that of the diffusion term $\vec{\nabla}\,\vec{J}_{X_i}$ tend to infinity. The calculations are performed assuming that the Maxwell-Boltzmann equilibrium is reached for the kinetic energy of atoms and molecules at T_A and electrons at T_e. These assumptions are verified a posteriori by comparing the characteristic time scale for reaching a Maxwellian equilibrium with that of the chemistry. Since the electrons are produced owing to the collisions resulting from the high temperature for heavy species, we can have $T_e \leq T_A$.
We can observe on Fig.17 and Fig.18 the time evolution of the number density of the species of Table 4 when a fluid particle with $T \simeq 200\,K$ crosses the shock front and is suddenly in high temperature ($7000\,K$ for Fig.17 and $10000\,K$ for Fig.18) and high pressure ($6\,kPa$ for Fig.17 and $15\,kPa$ for Fig.18) conditions. We can observe that the evolution of population densities starts immediately from $t = 0$ and stops at $\tau_c = 3\times10^{-5}\,s$ for $T_e = T_A = 7000\,K$ and at $\tau_c = 4\times10^{-4}\,s$ for $T_e = 5000\,K$ in the case of Fig.17. The fact that the evolution starts immediately from $t = 0$ is due to the very strong initial non equilibrium. The initial concentrations correspond as already mentioned to those before the shock front at high altitude typically where the temperature is approximately $T \simeq 200\,K$: there is no populated excited states in these conditions. As soon as the thermodynamic conditions change due to the crossing of the shock front, the density of species begin to evolve. When electrons and heavy species are in the same thermal conditions downstream the shock front, ($T_e = T_A$), τ_c is shorter and the state following this moment is quite close to chemical equilibrium, the pressure being sufficiently high. When $T_e < T_A$, this state is also quite close to chemical equilibrium and is almost the same than the latter. One of the important difference between both cases we can observe concerns τ_c. Although the electrons have a relatively weak influence on the final state, their density remaining low, decreasing their temperature T_e from $7000\,K$ to $5000\,K$ modifies τ_c by one order of magnitude. Figure 17 shows clearly that the negative charged particles are not electrons during the first part of the evolution ($t < 10^{-6}\,s$ to $10^{-5}\,s$ according to

the level of T_e). Changing T_e cannot therefore be ascribed to the action of the electrons. This behavior is in fact the result of the dissociation of N_2, O_2 and NO under their own impact which leads to higher concentrations observed before $10^{-7}\,s$ for $T_e = T_A$. Indeed, the rate coefficients that we use are derived from the paper of Losev and Shatalov (1990) and depends on both T_A and T_e assuming an equilibrium between the electrons and the vibration of the molecules.

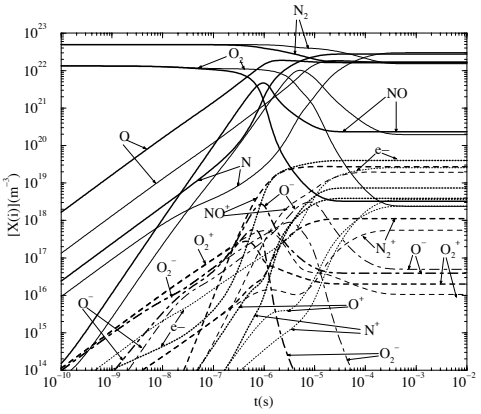

Figure 17: Time evolution in a typical reentry situation: ionization (thermal equilibrium: $T_e = T_A = 7000\,K$ in thick lines and $5000\,K = T_e < T_A = 7000\,K$ in thin lines for a case of thermal disequilibrium, negative ions in dot-dashed lines).

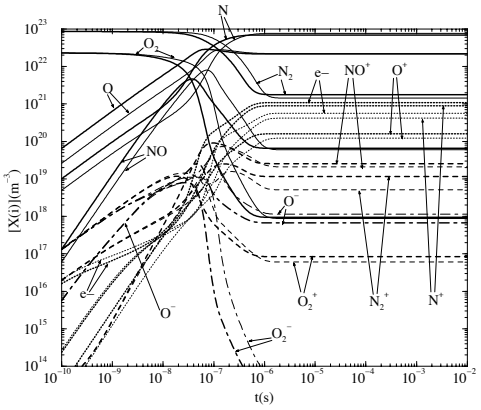

Figure 18: Time evolution in a typical reentry situation: ionization (thermal equilibrium: $T_e = T_A = 10000\,K$ in thick lines and $8000\,K = T_e < T_A = 10000\,K$ in thin lines for a case of thermal disequilibrium, negative ions in dot-dashed lines).

This hypothesis is highly questionable in the present case, the number density of electrons being very weak before $10^{-7}\,s$: this is confirmed by the evolution of $T_v^{NO^+(X)}$ displayed on Fig.19. This temperature is defined by:

$$T_v^{NO^+(X)} = -\frac{1}{k_B \left[\frac{d\ln([NO^+(X,v)]/Z_R(v))}{dE(X,v)}\right]_{lsl}} \tag{47}$$

where $Z_R(v)$ is the rotational partition function of the vibrational level v considered whose energy is $E(X,v)$ and lsl means that the derivative is in fact the slope of the least squares line.

Before $10^{-7}\,s$, the population density of the vibrational states are increasing and the efficiency of the elastic collisions with electrons or heavy particles is insufficient to ensure rapidly an equilibrium: the vibrational distribution does not follow a Boltzmann equilibrium neither with T_e nor T_A and depends on chemical processes. This is confirmed by Table 9 listing the main processes responsible for the creation and destruction for N, O, NO, O_2^-, O^-, electrons and NO^+ for $t \simeq 10^{-7}\,s$. This list shows clearly that populating the state $v = 0$ for $NO^+(X^1\Sigma^+)$ is dominated by associative ionization between O and $N(^2D)$ atoms and the inverse process of neutralization between NO^+ and O_2^- in a reduced

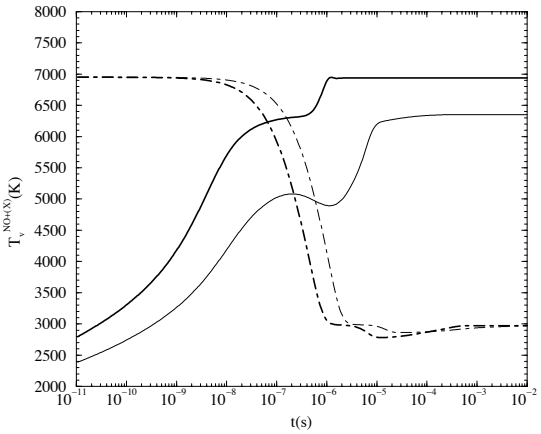

Figure 19: Time evolution of the vibrational temperature of $NO^+(X^1\Sigma^+)$ in the case of Fig.17, the gas having crossed the shock front and whose temperatures are such that $T_e = T_A = 7000\,K$ (thick line) or $5000\,K = T_e < T_A = 7000\,K$ (thin line). The thin dot-dashed line refers to the typical recombination inside the boundary layer with $p = 2\,kPa$ from $T_e = T_A = 7000\,K$ to $T_e = T_A = 3000\,K$ (see Fig.20 and 21) and the thick dot-dashed line refers to the same situation but with $p = 10\,kPa$ (see Fig.22 and 23).

Processes	(α)	(β)
$\rightarrow N$	$N_2 + O \rightarrow NO + N$	$N_2 + N_2 \rightarrow N + N + N_2$
$N \rightarrow$	$N + O_2 \rightarrow NO + O(^1D)$	$N + O_2 \rightarrow NO + O$
$\rightarrow O$	$O_2 + N_2 \rightarrow O + O + N_2$	$O_2 + O_2 \rightarrow O + O + O_2$
$O \rightarrow$	$O + N_2 \rightarrow O(^1D) + N_2$	$O + N_2 \rightarrow NO + N$
$\rightarrow NO$	$N_2 + O \rightarrow NO + N$	$O_2 + N \rightarrow NO + O(^1D)$
$NO \rightarrow$	$NO + N_2 \rightarrow N + O + N_2$	$NO + O \rightarrow O + O + N$
$\rightarrow O_2^-$	$O_2(a) + O^- \rightarrow O_2^- + O$	$O_2 + O_2 \rightarrow O_2^- + O_2^+$
$O_2^- \rightarrow$	$O_2^- + O_2 \rightarrow O_2 + O_2 + e^-$	$O_2^- + O \rightarrow O^- + O_2(a)$
$\rightarrow O^-$	$O_2 + e^- \rightarrow O^- + O$	$O_2^- + O \rightarrow O^- + O_2(a)$
$O^- \rightarrow$	$O^- + O_2(a) \rightarrow O_2^- + O$	$O^- + O \rightarrow O_2 + e^-$
$\rightarrow e^-$	$O_2 + O_2^- \rightarrow e^- + O_2 + O_2$	$O^- + O \rightarrow e^- + O_2$
$e^- \rightarrow$	$e^- + O_2 \rightarrow O^- + O$	$e^- + O_2^+ \rightarrow O + O(^1D)$
$\rightarrow NO^+$	$O + N(^2D) \rightarrow NO^+ + e^-$	$NO + O_2 \rightarrow NO^+ + O_2^-$
$NO^+ \rightarrow$	$NO^+ + N_2 \rightarrow NO^+(v = 1) + N_2$	$NO^+ + O_2 \rightarrow NO^+(v = 1) + O_2$

Table 9: Main processes at time $t = 10^{-7}\,s$ during the formation of the plasma illustrated by Fig.17 when $T_e = T_A$. The arrow indicates that the species X is produced ($\rightarrow X$) or destroyed ($X \rightarrow$). The second column (α) corresponds to the more efficient process and the third one (β) to that just follows. The species are on their ground state if there is no indication and NO^+ means $NO^+(X^1\Sigma^+, v = 0)$ except in the case $v = 1$.

way while populating the higher excited vibrational states are resulting from collisions with N_2 and O_2 molecules. Afterwards, elastic collisions with electrons remain not very efficient, n_e remaining relatively low: this is illustrated by Fig.17 where changing the electron temperature from $7000\,K$ to $5000\,K$ does not change $T_v^{NO^+(X)}$ by a same factor. Anyway, this behavior illustrates the high sensitivity of the kinetics towards the hypothesis adopted under high degree of non equilibrium and the limitations of our CR model.
Table 9 is also interesting because it provides understanding of the global mechanism of the plasma formation by coupling with Fig.17. Although the number density of O_2^- and O^- are completely negligible when the steady state is reached, these species play a key role in the ionization phase. It is often assumed that the ionization in shock waves is driven by associative ionization. When the gas contains molecules, they are dissociated under heavy particles impact and the atoms produced associate to form electrons. This is particularly true in the case of noble gases where atoms already exist: the associative ionization can start immediately (Drawin and Emard (1973)). We see that this is not the case for molecules being electronegative or having the possibility to form such species. The most important negative charged particles are O_2^- and O^- whose formation is derived from the charge transfer process $O_2(a) + O^- \rightarrow O_2^- + O$ and the inverse process of neutralization $O_2 + O_2 \rightarrow O_2^- + O_2^+$ for O_2^- and $O_2 + e^- \rightarrow O^- + O$ and the charge transfer process $O_2^- + O \rightarrow O^- + O_2(a)$ for O^-. These processes delay the formation of free electrons and form a reservoir which will be a subsequent source for these particles: in order of decreasing importance, the electrons are produced first by the process $O + O^- \rightarrow O_2 + e^-$ and second by the associative ionization $O + N(^2D) \rightarrow NO^+ + e^-$ at time $t = 2 \times 10^{-6}\,s$ for $T_e = T_A$. The numerical study of air shock waves do not usually involve these processes (Abe et al. (2002)). Nevertheless, it could be interesting to adopt them and observe their influence.
Apart from the problem of the vibrational distribution not necessarily in equilibrium during the first part of the evolution, the concentrations calculated for $t < 5 \times 10^{-8}\,s$ are not significant since it corresponds to too short time scales in regard to that for reaching Maxwellian equilibrium for electrons and heavy species. Moreover, assuming a linear decrease of the velocity through the shock front between v_∞ and v_Δ (see Fig.16) allows to estimate the duration of crossing the shock front (having a thickness equal to the mean free path λ under upstream conditions) of a fluid particle such that:

$$\tau_{sc} = \frac{\lambda}{v_\infty - v_\Delta} \ln \frac{v_\infty}{v_\Delta} \tag{48}$$

For a mean free path $\lambda \simeq 10^{-3}\,m$ in order of magnitude, we have $\tau_{sc} \simeq 10^{-6}\,s$. Before this value, the fluid particle is not yet in the conditions downstream the shock front and the calculation has to be considered prudently. Nevertheless, this calculation is interesting because it provides the chemical scheme leading to the formation of the plasma starting from a cold gas when the conditions change suddenly. Anyway, the state following τ_c is quite close to equilibrium: it depends very weakly on the initial conditions. Assuming once again a linear decrease of the speed from v_Δ to 0 between $y = \Delta$ and the wall, and assuming also that the cold gas is suddenly in the conditions just behind the shock front at $t = 0$, the y-location of the fluid particle at the time t is:

$$y(t) = \Delta\, e^{-v_\Delta\, t/\Delta} \tag{49}$$

When the near-equilibrium is reached (either at the time $\tau_c = 3 \times 10^{-5}\,s$ with $T_e = T_A = 7000\,K$ or at the time $\tau_c = 4 \times 10^{-4}\,s$ for the other case related to Fig.17), the fluid particle is located either in $y \simeq 6.3\,cm$ or in $y \simeq 0.8\,cm$ respectively. In both cases, one can conclude that the edge of the boundary layer is therefore close to chemical equilibrium because $y \geq \delta$.
The global behavior when $T_A = 10000\,K$ is the same as we can see on Fig.18. Due to strong non equilibrium, the time evolution starts immediately but stops approximately at the same time: when $t = \tau_c = 9 \times 10^{-7}\,s$ for $T_e = T_A = 10000\,K$ and when $t = \tau_c = 1.5 \times 10^{-6}\,s$ for $8000\,K = T_e < T_A = 10000\,K$. This is due to the same processes of dissociation discussed previously whose rate coefficient varies more slowly between $8000\,K$ and $10000\,K$ than between $6000\,K$ and $8000\,K$. As in that case, Fig.18 shows that the electrons are not the most significant negative charged particles. The first part of the evolution is also questionable regarding the characteristic time scales for reaching Maxwell-Boltzmann equilibrium for electrons and heavy species as well as regarding τ_{sc}, Eq.(48) leading to the estimation $\tau_{sc} = 2 \times 10^{-7}\,s$. The same conclusion can be derived from Eq.(49): whatever the conditions, the fluid particle is not still in the boundary layer when the near-equilibrium is reached: its location is $y \simeq 4.8\,cm$ for thermal equilibrium ($T_e = T_A = 10000\,K$) and is $y \simeq 4.7\,cm$ when $T_e = 8000\,K$. The chemical relaxation is therefore extremely rapid and the boundary layer's edge is therefore close to chemical equilibrium. Finally, the most important processes leading to the plasma formation are globally the same as those listed in Table 9.

4.3.2 Recombination situation

In the literature, different simplified kinetic schemes have been implemented in Navier-Stokes codes to study high temperature air flows and particularly boundary layers. Most of these schemes were developed during the 70's and 80's in the frame of the shuttle's building. We have chosen to discuss three widely used simplified kinetic schemes due to Dunn and Kang (1973), Gupta et al. (1990) and Park (1993), the latter being an up-dated version of an older one Park (1985). Except O_2^- and O^-, they consider the same species as those we have taken into account. In addition, apart from the scheme of Park, they assume a thermal equilibrium between electrons and heavy particles.
Conversely to the case of the kinetic scheme of Park, those of Dunn & Kang and Gupta contain the rate coefficient of each inverse process: as a result, we have calculated each inverse rate coefficient for the kinetic scheme of Park starting from the equilibrium constant. Its value is derived from his own work (Park (1990)) concerning the partition function of the involved species. In addition, all radiative processes have been removed in our CR model in order to test the kinetic scheme only.
The situations adopted for illustrating the difference between these schemes and our CR model are related to two pressure levels of $2\,kPa$ and $10\,kPa$ framing the typical range over which a re-entry occurs. In both cases, the plasma is initially at equilibrium with $T_e = T_A = 7000\,K$ and is recombining at $T_e = T_A = 3000\,K$. We can see on Fig.20 the time evolution of the neutral species and that of the charged species except electrons on Fig.21 calculated with our CR model and with the three other kinetic schemes. Figures 22 and 23 present the calculated evolutions in the same conditions but for $p = 10\,kPa$. Figure24 illustrates finally the time evolution of the electron density in the same thermal

conditions as previously considered with $p = 2\,kPa$ (α) and with $p = 10\,kPa$ (β).

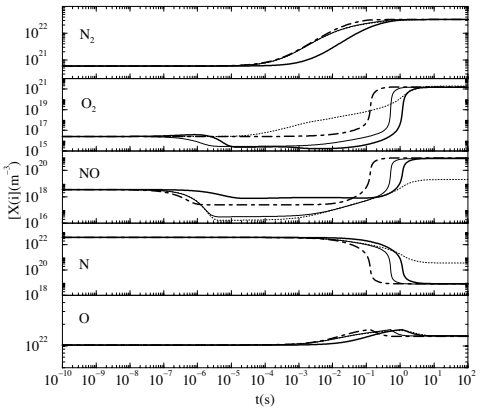

Figure 20: Time evolution of N_2, O_2, NO, N and O in a typical re-entry situation: recombination at $p = 2\,kPa$ from $T_e = T_A = 7000\,K$ to $T_e = T_A = 3000\,K$ (thick solid line: our model, thin solid line: Dunn & Kang, thin dotted line: Gupta, thick dot-dashed line: Park).

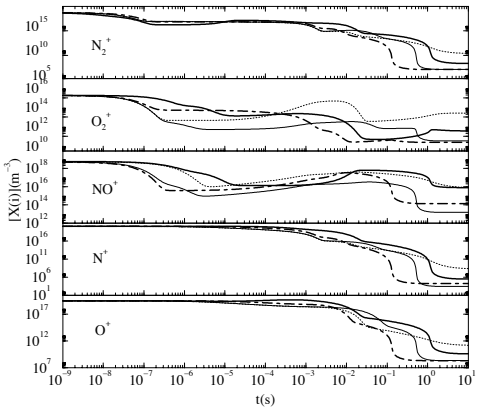

Figure 21: Time evolution of N_2^+, O_2^+, NO^+, N^+ and O^+ in a typical re-entry situation: recombination at $p = 2\,kPa$ from $T_e = T_A = 7000\,K$ to $T_e = T_A = 3000\,K$ (thick solid line: our model, thin solid line: Dunn & Kang, thin dotted line: Gupta, thick dot-dashed line: Park).

Since the plasma considered in this section is optically thick in order to make a comparison between chemical processes involved by the kinetic schemes only, the final state is an equilibrium state. The agreement is rather good for this final equilibrium state concerning N_2, O_2, NO, N and O except for the simplified kinetic scheme of Gupta which leads to a final overpopulation of N and to a final underpopulation of N_2 and NO. A calculation under a higher pressure condition as the atmospheric one show the same trend with in addition an overpopulation of O_2. This behavior is the direct result of the influence of the equilibrium constants. In particular, those of the Zeldovich's reaction (32a) is lower leading to a lower value for the rate coefficient in the case of the kinetic scheme of Gupta: the population density of O_2 and N are then higher while those of N_2 and NO are lower. We can observe for the ions on Figures 21 and 23 that their population density is of the same order of magnitude except for O_2^+ and NO^+. At atmospheric pressure, O_2^+ is overpopulated in the final equilibrium state in the case of the kinetic scheme of Gupta. This is also the direct result of the different equilibrium constants involved by each kinetic scheme. Moreover, we can observe that NO^+ is the more significant ion in the final equilibrium state: the temperature being relatively low, the number density of NO^+ is the highest one as a result of the high concentration of NO and its relatively low ionization characteristic temperature ($\simeq 107500\,K$).
The final electron density is in strong disagreement from a kinetic scheme to another.

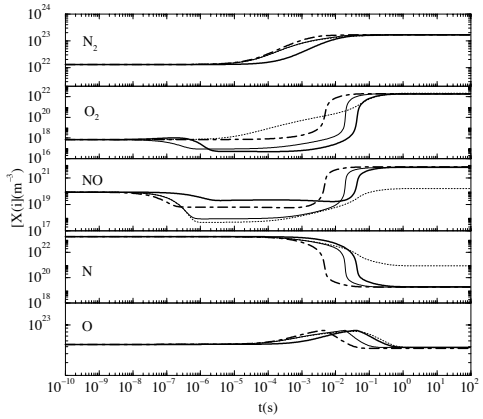

Figure 22: Time evolution of N_2, O_2, NO, N and O in a typical re-entry situation: recombination at $p = 10\,kPa$ from $T_e = T_A = 7000\,K$ to $T_e = T_A = 3000\,K$ (thick solid line: our model, thin solid line: Dunn & Kang, thin dotted line: Gupta, thick dot-dashed line: Park).

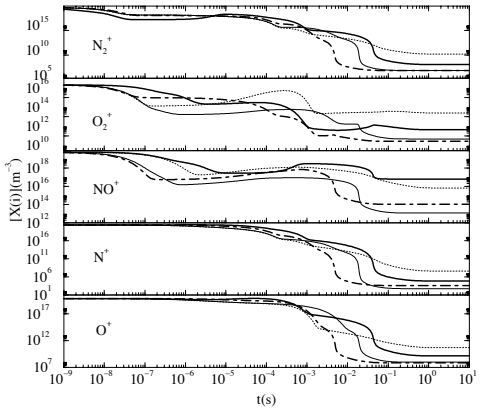

Figure 23: Time evolution of N_2^+, O_2^+, NO^+, N^+ and O^+ in a typical re-entry situation: recombination at $p = 10\,kPa$ from $T_e = T_A = 7000\,K$ to $T_e = T_A = 3000\,K$ (thick solid line: our model, thin solid line: Dunn & Kang, thin dotted line: Gupta, thick dot-dashed line: Park).

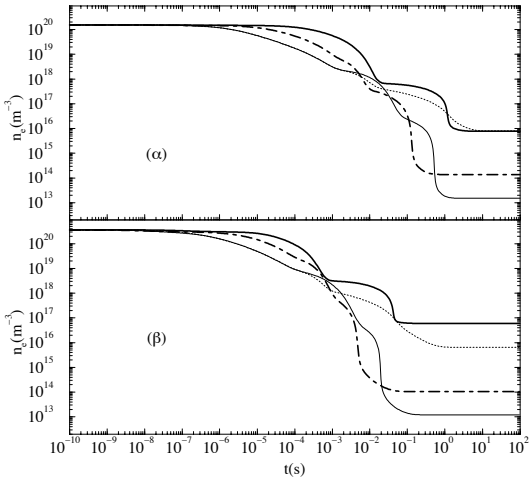

Figure 24: Time evolution of the electron density for a recombining plasma from $T_e = T_A = 7000\,K$ to $T_e = T_A = 3000\,K$ with $p = 2\,kPa$ (α) and with $p = 10\,kPa$ (β) (thick solid line: our model, thin solid line: Dunn & Kang, thin dotted line: Gupta, thick dot-dashed line: Park).

The reason can be ascribed once again to the equilibrium constants, but also to the electroneutrality: since NO^+ has the highest number density among the ions and since our kinetic scheme provides the highest population density for this molecular ion, the value of n_e in the final equilibrium state is then the highest one.
Although the final state is related with too long time scales with respect to the conditions typically involved in the re-entry conditions, nevertheless its study is very important: this informs about the quality of the equilibrium constants which are crucial because they provide the calculation of the inverse rate coefficients and consequently they influence the time evolution of the species number densities. The comparison between the good correlation of the final state for the neutral species and the bad one for that related to the charged species lead us to conclude that the equilibrium constants for the neutral species are better than for the charged ones.
Except the influence of the rate coefficients, the previous conclusion explain in part the fact that the different population densities evolve strongly in a different way during the transient step. We have already mentioned the influence of the rate coefficient for the Zeldovich's reaction (32a) which is very different from a kinetic scheme to another. The equilibrium constant being also different from a kinetic scheme to another, it is clear that the time evolution has no reason to be the same one. Nevertheless, the discrepancy is sometimes in a ratio higher than 50. For relatively short time scales as those related to typical re-entry ($\simeq 10^{-4}s$), the concentrations of O_2 and NO are very different.
In addition, this evolution depends strongly on the adopted initial conditions: equilibrium at $T = 7000\,K$ induces here higher concentrations for N^+ and O^+ than for NO^+: as a result, the latter ion plays a relatively minor role. For a lower temperature as considered in the next section, one have $[NO^+] = 4.9 \times 10^{18} m^{-3}$ at $T_e = T_A = 5400\,K$ while $[N^+] = 1.9 \times 10^{17} m^{-3}$ and $[O^+] = 2.4 \times 10^{17} m^{-3}$ when $p = 2\,kPa$ and $[NO^+] = 1.9 \times 10^{19} m^{-3}$, $[N^+] = 1.4 \times 10^{17} m^{-3}$ and $[O^+] = 3.5 \times 10^{17} m^{-3}$ when $p = 10\,kPa$. In this case, NO^+ is the more important ion and the recombination of electrons is driven essentially by its DR.
Figure 24 illustrates the evolution of n_e: the different kinetic schemes are globally in strong disagreement, even if the schemes of Dunn & Kang and Gupta are relatively well correlated for relatively short time scales. They underestimate clearly the electron density in relation to that calculated by the other schemes for $t < 10^{-4}\,s$ which is of interest in the case of a typical re-entry. In the case electrons play a role the temperature being sufficiently high, the kinetic scheme chosen to solve the boundary layer's equations will lead to very different results. We have made a special effort to describe correctly the recombination and as a result the ionization via the equilibrium constants: we can affirm that the recombination is too strong with the three common simplified kinetic schemes here studied.
Finally, Figure 19 shows that the relaxation of the vibrational distribution for $NO^+(X^1\Sigma^+)$ is almost complete when the transient regime begins for the other species: the assumption of a Maxwell equilibrium between the vibration of molecules with the other species is validated.

4.4 Conclusions

Three main conclusions can be derived from the study of the collisional radiative model for air. First, ionization situations have shown that O_2^- and O^-, due to their unsteady behavior, may have an influence on the characteristic time scale necessary to reach the equilibrium state. The common approach is to ignore these ions in shock layer computations. It could be interesting to account for them in a shock calculation.
The second important conclusion is that a CR model has to be time-dependent: it provides chemical characteristic time scales which can be compared with the other characteristic time scales of the flow. This temporal approach is also particularly powerful to check the quality of the equilibrium constants (by the equilibrium state finally reached and also by the transient regime).
Third, the comparison between the three common simplified kinetic schemes used for re-entry studies and the detailed CR model has shown that the results are very different from a scheme to another. This is the reason why it is clear that the better solution to validate a kinetic scheme is in fact to study the transient regime. We have shown that the final state allows to test the quality of the equilibrium constants only. The next step of this work is to derive a new simplified kinetic scheme to be implemented in a Navier-Stokes code devoted to re-entry studies. A time-dependent approach will allow to verify the relevance of this new reduced kinetic scheme over a wide temporal range.

5 Stagnation point boundary layer

A method has been proposed by researchers (Kolesnikov (1999)) at IPM (Moscow) to determine the catalytic properties of thermal protection systems (TPS). This method is indirect and is based on comparisons of the wall heat flux measured on a TPS sample set in a high enthalpy flow generated by a ICP torch with the flux calculated using a stagnation point boundary layer code. This method is popular and is used in different places in Europe, for example, at CORIA (France), VKI (Belgium) and in EADS-ST (France). Studies have been carried out for different materials. Most results available in the literature are for pure silica or for material containing mostly silica (e.g. RCG contains 92% silica). In this section, we present the stagnation point boundary layer code for air with different models for catalycity effects. Then for two typical flow conditions encountered in catalycity studies, the influence of the catalycity model and of the kinetic scheme is disccused.

5.1 Stagnation point boundary layer code

Classical boundary layer equations are written assuming that the flow is axisymmetric and laminar, dissociated but non ionized, in chemical nonequilibrium and in thermal equilibrium. Using the classical Lees-Dorodnitsyn $(x, y) \rightarrow (\xi, \eta)$ transformation, the boundary layer equations at the stagnation point reduce to a set of ordinary differential equations (Barbante (2001))

- continuity

$$\frac{\partial V}{\partial \eta} + f' = 0 \tag{50}$$

- momentum

$$V\frac{\partial f^{'}}{\partial \eta} = \frac{1}{2}\left(\frac{\rho_\delta}{\rho} - f^{'2}\right) + \frac{\partial}{\partial \eta}\left(l_0 \frac{\partial f^{'}}{\partial \eta}\right) \tag{51}$$

- species i continuity

$$V\frac{\partial y_i}{\partial \eta} + \frac{\partial J_i^\eta}{\partial \eta} = W_i \tag{52}$$

- energy

$$V\frac{\partial g}{\partial \eta} = \frac{\partial}{\partial \eta}\left(\frac{l_0}{Pr}\frac{\partial g}{\partial \eta}\right) - \frac{\partial}{\partial \eta}\left(\frac{l_0}{Pr}\sum_{i=1}^{N_s}\frac{\partial y_i}{\partial \eta}\frac{h_i}{h_\delta}\right) - \frac{\partial}{\partial \eta}\left(\sum_{i=1}^{N_s} J_i^\eta \frac{h_i}{h_\delta}\right) \tag{53}$$

with

$$f^{'} = \frac{u}{u_\delta} \tag{54}$$

and

$$g = \frac{h}{h_\delta} \tag{55}$$

where the subscript δ indicates a quantity evaluated at the boundary layer outer edge. y_i is species i mass fraction, u is the velocity component parallel to the wall and h is the enthalpy of the mixture. l_0 is defined as

$$l_0 = \frac{\rho\mu}{\rho_\delta \mu_\delta} \tag{56}$$

The local Prandtl number is

$$P_r = \frac{\mu c_p}{\lambda} \tag{57}$$

The dimensionless diffusion flux is

$$J_i^\eta = \frac{J_i^y}{\sqrt{2\rho_\delta \mu_\delta \frac{\partial u_\delta}{\partial x}}} \tag{58}$$

and the dimensionless mass production term is

$$W_i = \frac{w_i}{2\rho\frac{\partial u_\delta}{\partial x}} \tag{59}$$

where w_i is the mass source term of species i in the (x,y) framework.
In order to carry out a stagnation point boundary layer computation, it is necessary to know the wall temperature T_w and three parameters at the boundary layer edge: the velocity gradient $\beta = \frac{\partial u_\delta}{\partial x}$, T_δ and P_δ.
It is important to mention that to do comparisons with catalycity studies in subsonic flows generated by an ICP torch, the finite thickness of the boundary layer at low Reynolds numbers has to be taken into account (Barbante (2001)). Then, the set of equations for the stagnation point boundary layer has to be slightly modified. These corrections require to know precisely the boundary layer thickness and different velocity gradients. In this work, we propose to discuss the influence of different models on the results of the stagnation point boundary layer simulation, and therefore these corrections have been neglected.

5.1.1 Catalycity and boundary conditions

Catalycity effects are generally taken into account using two types of dimensionless coefficients: a recombination probability γ ($0 \leq \gamma \leq 1$) and an energy accommodation coefficient at the wall β. The γ_i coefficient for a species i is defined as

$$F_{i,recomb} = \gamma_i F_i \tag{60}$$

where F_i is the flux of species i impinging on the wall, and $F_{i,recomb}$ is the recombining flux of species i on the wall. Assuming a Boltzmann distribution of velocities close to the wall

$$F_i = n_i \sqrt{\frac{k_B T_w}{2\pi m_i}} \tag{61}$$

where m_i is the mass of species i. Then, the production rate of species i at the wall $w_{i,cat}$ can be written as

$$w_{i,cat} = \gamma_i m_i n_i \sqrt{\frac{k_B T_w}{2\pi m_i}} \tag{62}$$

The β coefficient is defined as

$$\beta = \frac{\dot{q}}{DF_{recomb}/2} \tag{63}$$

where $\dot{q}$ is the effective energy flux given to the wall, D is the dissociation energy of the molecule formed. Then the heat flux transferred to the wall depends on the product $\gamma^{'} = \gamma\beta$. It is interesting to note that $\gamma^{'}$ and γ are equal when the time of stay of the formed molecules on the surface is long enough. In this case, the whole recombination energy is given to the wall ($\beta = 1$). In fact, there has been only a few studies on the β coefficient determination and its modeling (Daiss et al. (1997); Scott (1990); Suslov and Tirskyi (1994); Barbato et al. (1998)), therefore generally this coefficient is assumed to be equal to 1 and only the γ coefficient is used. In this work, we have also used this approximation. Then, boundary conditions are written as
At the wall ($\eta = 0$)

$$u = v = 0 \tag{64}$$

$$h = h(T_w) \tag{65}$$

$$J^y_{i,w} = w_{i,cat} \tag{66}$$

where $J^y_{i,w}$ is the diffusion flux of species i in the direction normal to the wall. At the boundary layer edge ($\eta \to \infty$)

$$u = u_\delta \tag{67}$$

$$h = h_\delta = h(T_\delta, y_{i,\delta}) \tag{68}$$

$$y_i = y_{i,\delta} \tag{69}$$

The boundary layer flow is assumed to be in chemical equilibrium at the boundary layer edge, then $y_{i,\delta} = y_i(T_\delta, P_\delta)$. Finally, the wall heat flux is given by

$$q^y_w = -\lambda_w \left.\frac{\partial T}{\partial y}\right|_w + \left.\sum_{i=1}^{N_s} h_i J^y_i\right|_w \tag{70}$$

5.1.2 Thermochemical model

In the stagnation point boundary layer code, air is considered as a 5 species mixture (N_2, O_2, NO, N and O). To determine the viscosity and the thermal conductivity of the mixture, the mixing laws given by Gupta et al. (1990) have been used with the collision integrals calculated recently by Capitelli et al. (2000b). For boundary layer flows, it is particularly important to calculate accurately diffusion fluxes. The classical Fick's law gives a simple expression of diffusion fluxes. For example, the y component of the diffusion flux of species i in the mixture is

$$J_i^y = -\rho D_{im} \frac{\partial y_i}{\partial y} \tag{71}$$

where D_{im} is the diffusion coefficient of species i in the mixture. However, this simple expression does not satisfy the mass conservation: $\sum_{i=1}^{N_s} J_i^y = 0$ (unless all the D_{im} coefficients are equal) and therefore should not be used when diffusion processes are important. The rigorous expression of diffusion fluxes is given by Stefan - Maxwell and Sutton and Gnoffo (1998) have proposed an efficient iterative technique to determine them. In this case, the calculated fluxes satisfy the constraint of mass conservation.
In this work, the kinetic schemes proposed by Dunn and Kang (1973), Park (1993) and Gupta et al. (1990) adapted to a five species air mixture have been used.

5.1.3 Numerical method

The boundary layer equations (except the continuity equation) can be written in the generic form

$$a\frac{\partial^2 f}{\partial \eta^2} + b\frac{\partial f}{\partial \eta} + cf = d \tag{72}$$

with boundary conditions

$$\eta = 0 : a_l \frac{\partial f}{\partial \eta} + b_l f = c_l \tag{73}$$

$$\eta = \eta_\delta : f = f_\delta \tag{74}$$

and are solved with a 4th order finite difference method (Barbante (2001)). 500 points are taken in the η direction.

5.2 Catalycity models

5.2.1 Simplified models

The simplest model is to consider that only two recombination reactions occur at the wall (i.e. $N + N \rightarrow N_2$ and $O + O \rightarrow O_2$) and that these two reactions have the same γ coefficient. This model is widely used to determine an average γ coefficient for a material. From different measurements in pure nitrogen and oxygen flows, Scott (1990) and Kolodziej and Stewart (1987) have determined recombination rates of N in N_2 and O in O_2 on different surfaces as a function of the wall temperature T_w. Scott's fits for recombination coefficients are

$$\gamma_{NN} = 0.0714 e^{-2219/T_w}, \quad 950 < T_w < 1670K \tag{75}$$

$$\gamma_{OO} = 16.e^{-10271/T_w}, \quad 1400 < T_w < 1650K \tag{76}$$

Kolodziej and Stewart (1987) give

$$\gamma_{NN} = 0.061e^{-2480/T_w}, \quad 1410 < T_w < 1640K \tag{77}$$

$$\gamma_{OO} = 40.e^{-11440/T_w}, \quad 1435 < T_w < 1580K \tag{78}$$

These rates are usually implemented in air flow codes assuming that no NO is formed on the surface. They are very simple to use, but are valid in a small temperature range.

5.2.2 Phenomenological models

Different authors (Kovalev and Suslov (1996), Jumper and Seward (1994), Nasuti et al. (1996), Deutschmann et al. (1995) and Daiss et al. (1997)) have developed phenomenological models in which the gas-surface interaction is represented by different elementary reactions

- atom adsorption/desorption (Fig. 25)
- recombination of an atom of the gas with an atom adsorbed on the wall: Eley-Rideal (E-R) type process (Fig. 26)
- recombination of two adsorbed atoms at the wall: Langmuir-Hinshelwood (L-H) type process (Fig. 27)

For the temperatures and pressures studied, molecule adsorption at the wall is neglected. A rate coefficient is associated to each elementary process. In this case, the global γ' coefficient depends on temperature but also on the gas composition close to the wall.

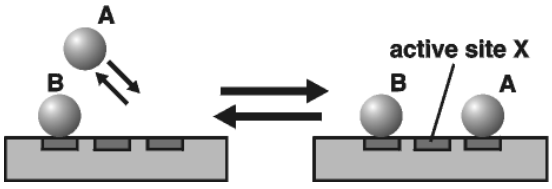

Figure 25: atom adsorption/desorption

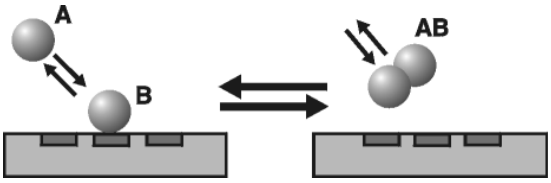

Figure 26: Eley-Rideal (E-R) type recombination process

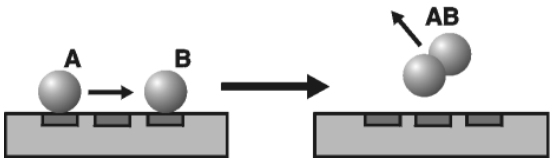

Figure 27: Langmuir-Hinshelwood (L-H) type recombination process

In the model derived by Deutschmann et al., simplified expressions for elementary rate coefficients are used. In works of Jumper et al., Daiss et al. and Nasuti et al., a better description of each process is given. In the model of Jumper et al., recombinations of O in O_2 and N in N_2 are assumed to be Eley-Rideal type processes. In the models of Daiss et al. and Nasuti et al., recombination reactions are assumed to be of both types. It is interesting to note that the model of Nasuti et al. takes into account the NO formation at the wall. In the model of Nasuti et al, the following processes are taken into account

- N and O atom adsorptions and desorptions

$$O + s \leftrightarrow O - s,\ N + s \leftrightarrow N - s \tag{79}$$

- Eley-Rideal type processes

$$O - s + O \leftrightarrow O_2 + s,\ N - s + N \leftrightarrow N_2 + s \tag{80}$$

$$O - s + N \leftrightarrow NO + s,\ N - s + O \leftrightarrow NO + s \tag{81}$$

- Langmuir-Hinshelwood type processes

$$O - s + O - s \leftrightarrow O_2 + 2s,\ N - s + N - s \leftrightarrow N_2 + 2s \tag{82}$$

$$O - s + N - s \leftrightarrow NO + 2s \tag{83}$$

where s is a free surface site. With this approach, it is necessary to define four recombination probabilities at the wall : γ_{OO}, $\gamma_{NN}, \gamma_{NO}, \gamma_{ON}$.

Expressions of γ coefficients

Due to a competition between O and N recombination processes at the wall, the four recombination probabilities are not independent of each other. Therefore γ_{NN} and γ_{OO} coefficients obtained in pure nitrogen and oxygen flows certainly overestimate these coefficients in an air flow where both atoms are present. Furthermore, the number of surface sites for N and O adsorption may be limited due to the chemisorption on the surface of other species such as the H_2O molecule which forms Si-OH bounds on a silica surface. To determine, the surface coverage rate by OH, Nasuti et al. proposes

$$\theta_{OH} = A(1 - exp(-E_{OH}/k_B T)) \tag{84}$$

The surface coverage rates θ_O et θ_N are related to the free surface sites θ_f by

$$\theta_f = 1 - \theta_O - \theta_N - \theta_{OH} \tag{85}$$

with $0 \leq \theta_f \leq 1$. At the stationary state, the number of adsorbed atoms on the surface is constant and therefore, the flux of adsorbed atoms i on the surface (F_{ai}) is equal to the flux of atoms recombining following a L-H (F_{lhii}) or a E-R (F_{erii}) process and to the flux of atoms thermally desorbed (F_{tdii}). Then, for O and N we have

$$F_{aO} = F_{erNO} + F_{erOO} + F_{lhNO} + F_{lhOO} + F_{tdO} \tag{86}$$

$$F_{aN} = F_{erON} + F_{erNN} + F_{lhNO} + F_{lhNN} + F_{tdN} \tag{87}$$

As we will see in the following, these different fluxes are functions of the two variables θ_O and θ_N. The system of equations (86) and (87) is therefore a quadratic system of equations for θ_O and θ_N variables which can be easily solved by an iterative method (e.g. Newton-Raphson method). When θ_O et θ_N are known, the different recombination probabilities can be expressed as

$$\gamma_{OO} = \frac{(F_{lhOO} + 2F_{erOO})}{F_O} \tag{88}$$

$$\gamma_{NN} = \frac{(F_{lhNN} + 2F_{erNN})}{F_N} \tag{89}$$

$$\gamma_{ON} = \frac{(F_{lhNO} + F_{erNO} + F_{erON})}{F_O} \tag{90}$$

$$\gamma_{NO} = \frac{(F_{lhNO} + F_{erNO} + F_{erON})}{F_N} \tag{91}$$

These four coefficients depend on p_O, p_N, θ_N, θ_O and T.

Wall boundary conditions for the different species

The production rate $w_{i,cat}$ at the wall of species $i = N_2, O_2, NO, N$ and O can be written as

$$w_O = m_O(\gamma_{OO} + \gamma_{ON})F_O \tag{92}$$

$$w_N = m_N(\gamma_{NN} + \gamma_{NO})F_N \tag{93}$$

$$w_{O_2} = -m_O\gamma_{OO}F_O \tag{94}$$

$$w_{NO} = -(m_O\gamma_{ON}F_O + m_N\gamma_{NO}F_N) \tag{95}$$

$$w_{N_2} = -m_N\gamma_{NN}F_N \tag{96}$$

where F_i is the flux of species i impinging on the wall and is given by Eq. (61). The flux of atoms i adsorbed at the wall F_{ai} is proportional to F_i and to the number of free surface sites θ_f

$$F_{ai} = s_i\theta_f F_i \tag{97}$$

where s_i is a sticking coefficient ($0 \leq s_i \leq 1$). The flux F_{erij} of atoms i in the gas, recombining with adsorbed atoms j to form an ij molecule following an E-R process is proportional to F_i and θ_j

$$F_{erij} = \gamma^*_{ij}\theta_j F_i \tag{98}$$

where $0 \leq \gamma^*_{ij} \leq 1$ with:

$$\gamma^*_{ij} = P_{erij}exp(-Q_{erij}/k_BT) \tag{99}$$

In a L-H recombination process, both atoms are adsorbed at the wall. The flux of adsorbed atoms which recombine following a L-H type process to form O_2, N_2 and NO are respectively

$$Z_{lhOO} = 2\nu_O n\theta_O^2 exp[-(Q_{lhOO}/k_BT)] \tag{100}$$

$$Z_{lhNN} = 2\nu_N n\theta_N^2 exp[-(Q_{lhNN}/k_BT)] \tag{101}$$

$$Z_{lhNO} = (\nu_N + \nu_O) n \theta_N \theta_O exp[-(Q_{lhNO}/k_B T)] \quad (102)$$

where n is the number of surface sites per unit surface and ν_i is a characteristic frequency given by

$$\nu_i = (c_A/\Delta)\sqrt{\pi k_B T/2m_i} \quad (103)$$

where Δ is the mean distance between surface sites and c_A is a constant. Activation energies are given by

$$Q_{lhOO} = MAX(2Q_{aO} - D_{OO}, E_{mO}) \quad (104)$$

where Q_{ai} is the surface-atom bond energy for atom i and E_{mi} is the energy necessary for species i to move on the surface and D_{ij} is the bond energy between i and j atoms.

$$Q_{lhNN} = MAX(2Q_{aN} - D_{NN}, E_{mN}) \quad (105)$$

$$Q_{lhNO} = Q_{aO} + Q_{aN} - D_{NO} \quad (106)$$

The flux of thermal desorption F_{tdi} is

$$F_{tdi} = n\theta_i (k_B T/h) exp[-Q_{tdi}/k_B T)] \quad (107)$$

where Q_{tdi} is an activation energy.

Wall	
n	$4.510^{18} m^{-2}$
Δ	$510^{-10} m$
For N	
E_{mN}	$82.2 kJ/mol$
Q_{aN}	$530.8 kJ/mol$
D_{NN}	$941.3 kJ/mol$
For O	
E_{mO}	$159.1 kJ/mol$
Q_{aO}	$499.8 kJ/mol$
D_{OO}	$498 kJ/mol$

Table 10: Data for the model derived by Nasuti et al. (1996).

For N	
s_N	0.015
P_{erNN}	0.1
Q_{erNN}	$20 kJ/mol$
Q_{tdN}	Q_{aN}
For O	
s_O	0.05
P_{erOO}	0.1
Q_{erOO}	$20 kJ/mol$
Q_{tdO}	$Q_{aO}/2.$
c_A	3.5
For OH	
A	1.
E_{OH}	$2.5 kJ/mol$

Table 11: Parameters derived to have the best agreement with experimental results obtained in pure nitrogen and oxygen flows (Nasuti et al. (1996)).

Determination of the parameters of the model

Among the different parameters of the model, there are:

- parameters which depend on the model chosen for the surface : Q_{ai}, Δ, n and E_{mi}

- fundamental data available in the literature as bond energies D_{ij}
- parameters which can be derived from semi-empirical models : Q_{erij}, Q_{ai} and Q_{tdi},
- parameters for which no theoretical model is available: P_{erij}, s_i and c_A.

The three first types of parameters are given in table 10. Figure 28 shows numerous measurements reviewed by Jumper and Seward (1994) and Wiley (1993) of γ_{NN} et γ_{OO} for pure silica or RCG in pure nitrogen and oxygen flows. These results have been used to determine the parameters of the model given in table 11. For the thermal desorption threshold, we have assumed that $Q_{tdN} = Q_{aN}$ and Q_{tdO} is taken equal to $Q_{aO}/2$ to have a maximum of γ_{OO} at $T \simeq 1600K$. On Fig. 28, the results obtained by the model proposed by Jumper are also shown. In this model, recombination processes are of the E-R type and P_{erij} and s_i are assumed to depend on the temperature. Experimental results seem to indicate that γ_{OO} has a maximum at $T \simeq 1600K$. This evolution is well reproduced by both models and is due to thermal desorption which becomes very efficient as temperature increases. With the model of Nasuti, γ_{OO} is independent of pressure for $T < 1000K$ and depends on the pressure for higher temperatures. For O in O_2 recombination, we have checked that in the studied wall temperature range $300K - 2000K$, the L-H type process is negligible, and then the recombination process is an E-R type recombination process. For γ_{NN}, experimental data are scarce and therefore the existence of a maximum at $T \simeq 1600K$ is not obvious. This maximum exists in the model of Jumper but not in the model of Nasuti. With the model of Nasuti, γ_{NN} depends on pressure only for $600K < T_w < 1000K$. For $T < 600K$, the recombination process is an E-R type process and it is a L-H process for $T > 1000K$. For air, no measurements of the different γ coefficients are available. For the recombination of O in O_2 and of N in N_2, the parameters derived hereabove are used. The other parameters are given in table 12 following the assumptions of Nassuti et al.

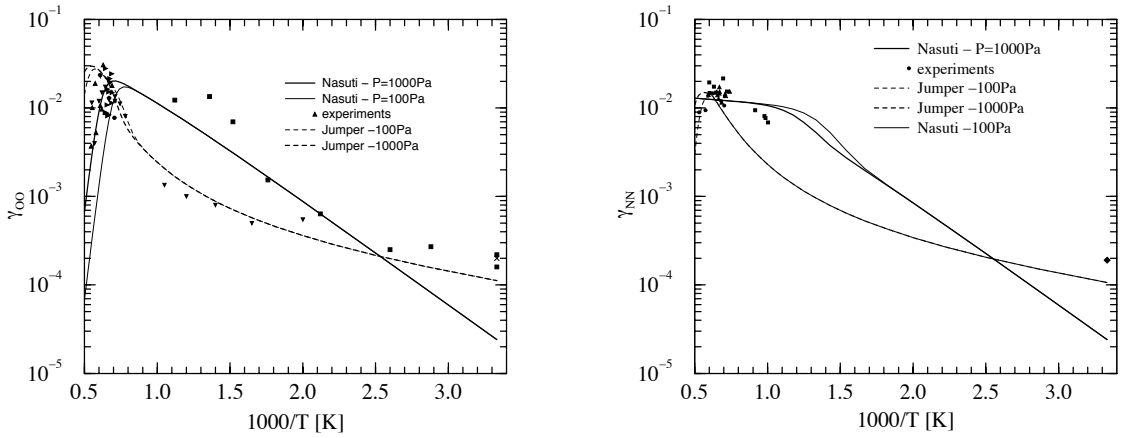

Figure 28: Recombination probabilities of N in N_2 and of O in O_2 on pure silica and RCG. Symbols correspond to different experimental results reviewed in Jumper and Seward (1994) and Wiley (1993).

For ON	
Q_{erON}	Q_{erNN}
P_{erON}	P_{erNN}
For NO	
Q_{erNO}	Q_{erOO}
P_{erNO}	P_{erOO}
D_{NO}	$625.1kJ/mol$

Table 12: Parameters for ON and NO (Nasuti et al. (1996)).

5.3 Results

In this section, we present results for two typical conditions of catalycity studies carried out in high enthalpy flows generated by a ICP torch. For both test-cases, we propose to discuss the influence of the model used for catalycity and for the gas kinetic scheme on the calculated results.

5.3.1 High pressure test case : $P = 10000Pa$

We consider typical boundary edge conditions at $P_\delta = 10000Pa$: $T_\delta = 4500K$ and $\beta = 11600s^{-1}$ (Barbante (2001)). The simplest model for catalycity presented in Section 5.2.1 is to consider that only two recombination reactions occur at the wall (i.e. $N + N \rightarrow N_2$ and $O + O \rightarrow O_2$) and that these two reactions have the same γ coefficient. Figure 29 presents the wall heat flux as a function of the wall temperature for different values of γ. In the classical method derived by IPM to determine the catalycity of a TPS, measured heat fluxes are set in this figure to determine the γ coefficient of the studied wall.
As expected the calculated wall heat flux increases as γ increases and as the wall temperature decreases. For a given wall temperature, the heat flux in the fully catalytic case is about twice the flux in the noncatalytic case. The heat flux for a fully frozen flow (i.e. no reactions in the gas and at the wall) is also shown. This flux is the lower heat flux limit. In the noncatalytic case, the difference between the flux calculated in the frozen case and the curve denoted $\gamma = 0$, shows the influence of the gas chemistry on the heat flux. Figure 29 shows that this influence decreases as the wall temperature increases, as the recombination of atoms in the gas is more efficient at low temperature. Figure 30 presents the wall heat flux calculated using the phenomenological model derived by Nasuti et al and presented in Section 5.2.2 . At low temperature, this model shows that the wall is noncatalytic and that its catalycity increases up to $T_w \simeq 1400K$. For higher temperatures, thermal desorption becomes very efficient and the calculated wall heat flux decreases.

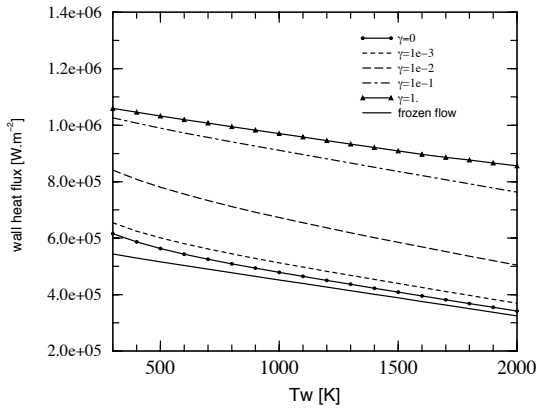

Figure 29: Wall heat flux as a function of the wall temperature for different values of the average γ coefficient. The kinetic scheme of Dunn and Kang is used.

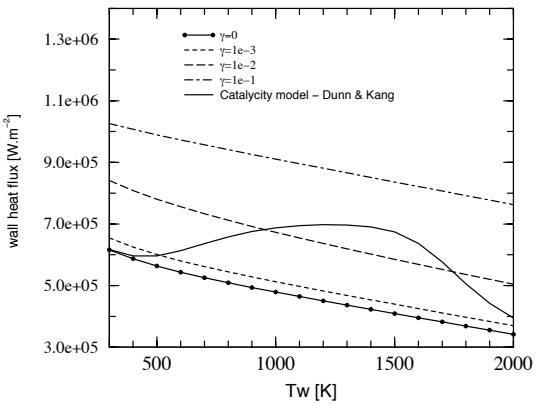

Figure 30: Same as Fig. 29 with the heat flux calculated using the phenomenological model derived by Nasuti et al.

Figure 31 shows that the γ coefficients of the different species calculated with the phenomenological model have very different values from each other and different evolutions with the wall temperature. At low temperature $T_w \leq 1000K$, γ_{OO} and γ_{NO} are close to each other and much higher than the two other coefficients. The γ_{NN} coefficient increases as the wall temperature increases and becomes the highest recombination coefficient for $T_w \geq 1800K$. We note that the γ_{ON} remains very small in the whole temperature range.

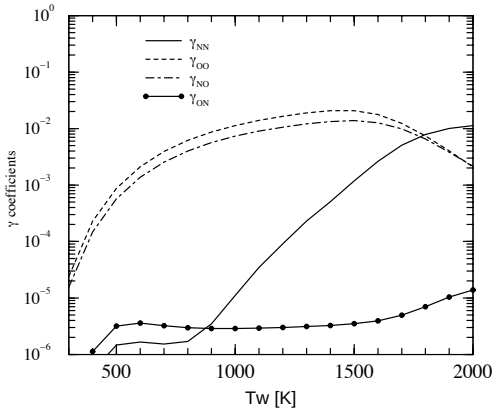

Figure 31: γ coefficients of the phenomenological model derived by Nasuti et al. for the conditions of Fig. 30.

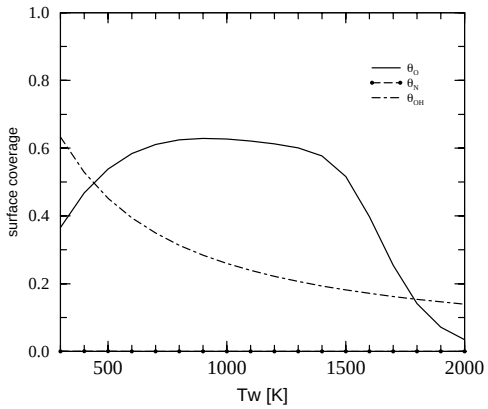

Figure 32: Different values of θ coefficients for the same condition as Fig. 31.

Figure 32 shows the surface coverage for O, N atoms and the OH molecule for the conditions of Fig. 31. The surface coverage by the OH molecule decreases as the wall temperature increases. The surface coverage by O atoms is on the average of 0.5 for

$300K \leq T_w \leq 1500K$ and then decreases rapidly for higher temperature due to thermal desorption. The N atom surface coverage remains very small in the whole temperature range.

Figure 33 shows the species concentration for $T_w = 1500K$ and the phenomenological model proposed by Nasuti et al. Strong variations are observed close to the wall for N, O_2 and NO. Figure 33 compares the wall heat flux calculated with the phenomenological model proposed by Nasuti et al. using different kinetic schemes (Dunn and Kang , Park and Gupta) and for a frozen flow. In the scheme of Park, backward rate coefficients are derived from forward rates using equilibrium constants fitted as a function of temperature for $T \geq 500K$. To avoid numerical problems at low temperatures with these fits, we present results for the kinetic scheme of Park for $T \geq 1000K$. The heat fluxes calculated using the kinetic scheme of Dunn and Kang are very close to the results obtained for the scheme of Gupta for $T > 700K$. The most significant discrepancies are observed for lower temperatures. The heat fluxes calculated using Park's kinetic scheme are slighlty higher than those obtained with Dunn and Kang scheme but the discrepancy remains small. The heat flux calculated assuming a frozen flow is the lower heat flux limit. We note that the discrepancies with the results obtained assuming a reacting boundary layer are rather small and decrease as the wall temperature increases. Then, for wall temperatures $T_w \simeq 1500K$ usually encountered in catalycity studies, the flow is nearly frozen at $P = 10000Pa$. Figure 34 also shows the heat flux calculated using the kinetic scheme of Dunn and Kang and Fick's law for diffusion fluxes. In this case, the influence of the modeling of the diffusion flux appears to be rather small and the use of Fick's law slightly overestimates the calculated wall heat flux.

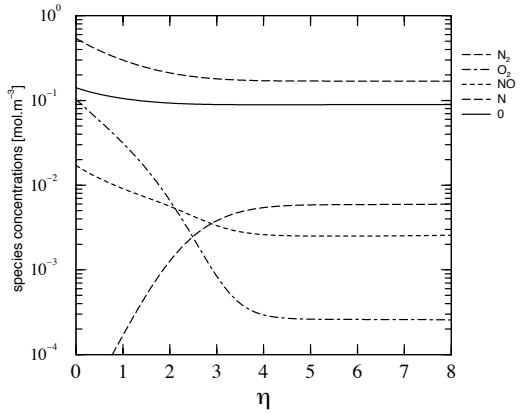

Figure 33: Species concentrations in the boundary layer for $T_w = 1500K$ using the phenomenological model. The kinetic scheme of Dunn and Kang is used.

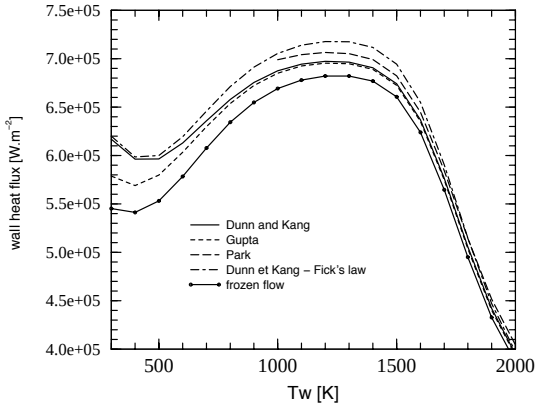

Figure 34: Wall heat flux calculated for different gas kinetic schemes and with the kinetic scheme and Dunn and Kang and the simple Fick's law for diffusion fluxes.

5.3.2 Low pressure test-case : $P = 2000Pa$

We consider typical boundary edge conditions at $P_\delta = 2000Pa$: $T_\delta = 5400K$ and $\beta = 14000s^{-1}$ (Bourdon et al. (2003)).

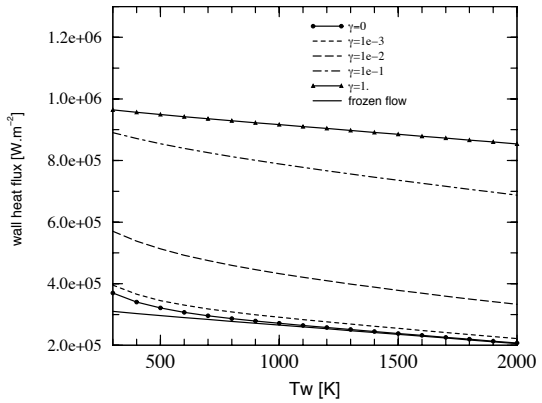

Figure 35: Wall heat flux as a function of the wall temperature for different values of the average γ coefficient. The kinetic scheme of Dunn and Kang is used.

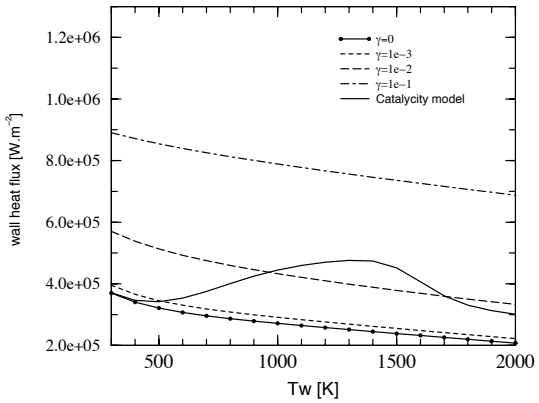

Figure 36: same as Fig. 35 with the heat flux calculated using the phenomenological model derived by Nasuti et al.

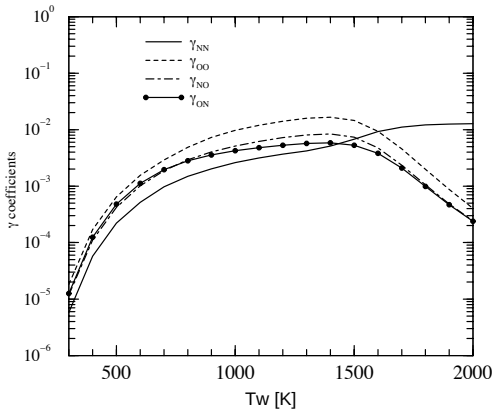

Figure 37: γ coefficients of the phenomenological model derived by Nasuti et al. for the conditions of Fig. 36.

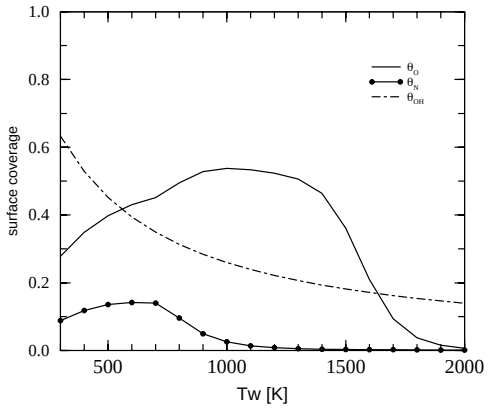

Figure 38: Different values of θ coefficients for the same condition as Fig. 37.

Figure 35 presents the wall heat flux as a function of the wall temperature for different values of γ and Fig. 36 shows the flux obtained using the phenomenological model derived by Nasuti et al. As for the high pressure case, we note a strong nonlinear dependence of

the heat flux with the recombination probability γ. The heat flux for a fully frozen flow (i.e. no reactions in the gas and at the wall) is also shown. The difference of this flux with the one denoted $\gamma = 0$, puts forward (as already observed for the high pressure case) that for $P_\delta = 2000Pa$ in the noncatalytic case, the influence of the chemistry on the heat flux decreases as the wall temperature increases. Figure 37 shows that γ coefficients of the different species calculated with the phenomenological model. The coefficients γ_{OO}, γ_{NO} and γ_{ON} have a similar evolution with temperature. They increase up to $T_w \simeq 1500K$ and decrease for higher temperatures. For $300K \leq T_w \leq 2000K$, γ_{NN} increases with the temperature and for $T_w \geq 1700K$, this is the highest recombination coefficient. We note that the γ_{ON} coefficient is much higher in this condtion at $P_\delta = 2000Pa$ than for the previous case at $P_\delta = 10000Pa$. Figure 38 shows the surface coverage for O, N atoms and the OH molecule for the conditions of Fig. 37. The surface coverage by the OH molecule decreases as the wall temperature increases. The surface coverage by O atoms is rather high for $300K \leq T_w \leq 1500K$ and then decreases rapidly for higher temperature due to thermal desorption. The N atom surface coverage remains small in the whole temperature range but is much higher for $T_w \leq 1000K$ in this case than in the previous case at $P_\delta = 10000Pa$.

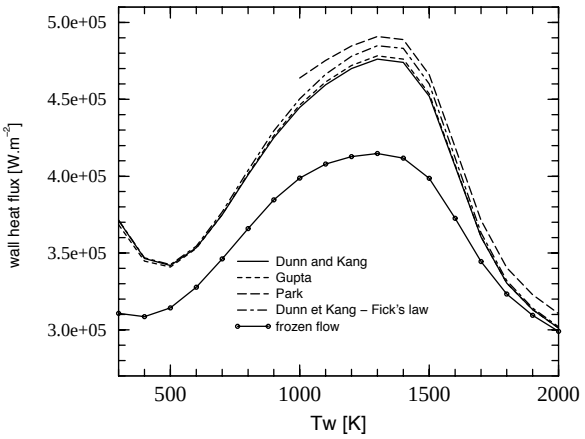

Figure 39: Wall heat flux calculated for different gas kinetic schemes and with the kinetic scheme and Dunn and Kang and the simple Fick's law for diffusion fluxes.

Figure 39 compares the wall heat flux calculated with the phenomenological model proposed by Nasuti et al. using different kinetic schemes (Dunn and Kang , Park and Gupta) and for a frozen flow. The heat fluxes calculated using the kinetic scheme of Dunn and Kang are very close to the results obtained for the scheme of Gupta for the whole temperature range. The heat fluxes calculated using Park's kinetic scheme for $T_w \geq 1000K$ are slightly higher than those obtained with Dunn and Kang scheme but the discrepancy remains small. The heat flux calculated assuming a frozen flow is the lower heat flux limit. We note that the discrepancy with the results obtained assuming a reacting boundary layer is of about 20% for $T_w = 300K$, 15% for $T_w = 1300K$ and decreases for higher

temperatures. We note that the influence of the gas chemistry on the calculated heat flux appears to be more significant for the boundary layer conditions at $P_\delta = 2000Pa$ than at $P_\delta = 10000Pa$. Therefore, for wall temperatures $T_w \simeq 1500K$ usually encountered in catalycity studies, the chemistry of the gas has a non negligible influence at $P_\delta = 2000Pa$ on the catalycity coefficients derived for the material. Figure 39 also shows the heat flux calculated using the kinetic scheme of Dunn and Kang and Fick's law for diffusion fluxes. In this case, the influence of the modeling of the diffusion flux appears to be rather small and the use of Fick's law slightly overestimates the calculated wall heat flux.
Figure 40 shows the species concentrations for $T_w = 1500K$ and the phenomenological model proposed by Nasuti et al. We note that the evolution of the different species concentrations in the boundary layer is very different than the one obtained for $10000Pa$. Figure 41 shows the species concentrations for the same boundary conditions, but a frozen chemistry. We note that a 15% difference on the wall heat flux (Figure 39) corresponds to significant discrepancies on the different species evolutions in the boundary layer. It would be very interesting to compare these results with species concentrations measurements in the boundary layer.

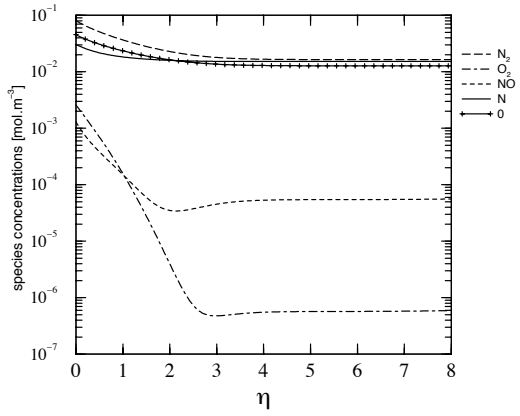

Figure 40: Species concentrations in the boundary layer for $T_w = 1500K$ using the phenomenological model. The kinetic scheme of Dunn and Kang is used.

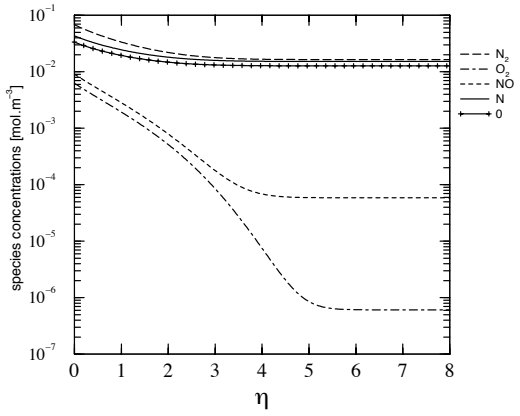

Figure 41: Species concentrations in the boundary layer for $T_w = 1500K$ using the phenomenological model. The boundary layer is assumed to be frozen.

6 Conclusions

Two main conclusions can be derived from the work developed in the previous sections on (1) the gas phase chemistry and on (2) the interaction between a gas and a surface during the re-entry of a spacecraft into the upper layers of the earth's atmosphere.
First, the elaboration of a relevant and detailed kinetic scheme for a given gas phase is a difficult task which has to be done carefully, since numerous species and elementary processes are involved. For each process a rate coefficient has to be found and it is important to try to find the most accurate theoretical or experimental data. The chemistry being

time-dependent by nature, it is important to take into account species that may play a role in the time evolution even if their concentration at the stationary state is negligible. Furthermore, it is important to be able to reduce the kinetic scheme after having carefully compared the results of the simplified scheme with the detailed scheme.
We have used this procedure to derive the three-body recombination and effective ionization rate coefficients of atomic oxygen from a detailed collisional radiative model. The time-dependent approach used in this work has clearly put forward the necessity that the system be in a quasi-steady state to derive meaningful rate coefficients. In addition, we have also shown that the value of these rate coefficients depends on the number of excited levels considered. Then, to elaborate a CR model for air, we have shown that it is necessary to take into account a sufficient number of excited levels in order to calculate correctly the ionization or recombination as well as all processes occurring in this type of medium. The results obtained put forward significant discrepancies with common simplified kinetic schemes used for re-entry studies. The CR scheme developed in this work can be used to derive up-dated and new simplified kinetic schemes for air for various applications. For the validation of a simplified kinetic scheme, we recommend careful comparisons of the time-dependent results obtained with the simplified scheme and with the CR model.
Second, the stagnation point boundary layer study has shown that the problem of the determination of the catalycity of the surface interacting with a re-entry plasma is far from being solved. The surface chemistry plays a crucial role and the net heat flux is highly dependent on the surface temperature. We have shown that the chemistry of the gas phase plays a non negligible role in particular for $P \leq 10000Pa$. For the conditions studied in section 5 the discrepancies between different kinetic schemes remain small, as the temperature in the boundary layer remains less than $5400K$. However, the time-dependent CR model has put forward that these discrepancies may be significant when the temperature in the boundary is high enough to have a non negligible ionization degree.
In this work, we have used a phenomenological model for wall catalycity. We have shown that this type of model gives very interesting information on the evolution of the catalycity with the wall temperature. It would be interesting to further improve the modeling of the gas surface interaction in flow and boundary layer codes. For example it could be very interesting to take into account the dynamics of the lattice atoms according to the semi-classical collisional method, which has been developed and successfully applied for the description of oxygen recombination on silica surfaces (Cacciatore et al. (1999)).
Finally, to validate the results obtained, a comparison with experiments is necessary. However, it is difficult to measure the concentrations of a large number of species in a flow simple enough to be a good test-case to validate accurately a nonequilibrium chemistry. For catalycity studies, up to now, only a limited number of parameters have been measured in the stagnation point boundary layer and at the wall. It would be interesting to carry out further measurements of the evolutions of different species concentrations in the boundary layer to better validate the results.

References

Abe, K., Kihara, H., Uchida, T., and Nishida, M. (2002). Experimental and numerical studies of rotational relaxation behind a strong shock wave in air. *Shock Waves*, 11:413.

Anderson, J. (1989). *Hypersonic and High Temperature Gas Dynamics*. McGraw-Hill Book Company, New York.

Armenise, I., Capitelli, M., Colonna, G., and Gorse, C. (1996). Nonequilibrium vibrational kinetics in the boundary layer of re-entering bodies. *Journal of Thermophysics and Heat Transfer*, 10(3):397.

Barbante, P. (2001). *Accurate and efficient modelling of high temperature nonequilibrium air flows*. PhD thesis, VKI, Université libre de Bruxelles, Belgique.

Barbato, M., Belluci, V., and Bruno, C. (1998). Effects of catalytic boundary conditions accounting for incomplete chemical energy accomodation. AIAA Paper 98-2846.

Bardsley, J. (1983). Dissociative recombination of electrons with no^+ ions. *Planet and Space Science*, 31(6):667.

Bates, D., Kingston, A., and McWhirter, R. (1962). Recombination beween electrons and atomic ions i. optically thin cases. *Proceedings of the Royal Society of London*, 267:297–312.

Berrington, A.K. and Burke, P.G. and Robb, W.D. (1975). The scattering of electrons by atomic nitrogen. *Journal of Physics B: Atomic and Molecular Physics*, 8(15):2500–2511.

Bhatia, A. and Kastner, S. (1995). The neutral oxygen spectrum 1: Collisionally excited level populations and line intensities under optically thin conditions. *Astrophysical Journal Supplement Series*, 96(1):325–341.

Biémont, E. and Zeippen, C. (1992). Electric dipole transitions in atomic oxygen and lifetimes of the 2p3 (4s) 3s 5s and 3s states. *Astronomy and Astrophysics*, 265:850–856.

Billing, G. and Fisher, E. (1979). Vv and vt rate coefficients in n_2 by a quantum-classical model. *Chemical Physics*, 43:395.

Bose, D. and Candler, G. (1996). Thermal rate constants of the $n_2 + o \rightarrow no + o$ reaction using *ab initio* $^3a"$ and $^3a'$ potential-energy surfaces. *Journal of Chemical Physics*, 104(8):2825.

Bose, D. and Candler, G. (1997). Thermal rate constants of the $o_2 + n \rightarrow no + o$ reaction based on the $^2a'$ and $^4a'$ potential-energy surfaces. *Journal of Chemical Physics*, 107(16):6136.

Bourdon, A., Bultel, A., Desportes, A., and Vervisch, P. (2003). Cnes-nasda-coria collaboration on catalycity : γ coefficient determination of c/c samples at coria. Technical report.

Bourdon, A., Térésiak, Y., and Vervisch, P. (1998). Ionization and recombination rates of atomic oxygen in high temperature air plasma flows. *Physical Review E*, 57(4):4684–4692.

Bourdon, A. and Vervisch, P. (1996). Three body recombination rate of atomic nitrogen in low-pressure plasma flows. *Physical Review E*, 54(2):1888–1898.

Bultel, A., van Ootegem, B., Bourdon, A., and Vervisch, P. (2002). Influence of ar_2^+ in an argon collisional-radiative model. *Physical Review E*, 65:046406.

Cacciatore, M. and Capitelli, M. (1976). The temporal evolution of population densities of excited states in atomic oxygen thin plasmas. *Journal of Quantitative Spectroscopy and Radiative Transfer*, 16(4):325–334.

Cacciatore, M., Rutigliano, M., Billing, G.D. (1999). Elley-Rideal and Langmuir-Hinshewood recombination coefficients for oxygen on silica surfaces. *Journal of Thermophysics and Heat Transfer*, 13(2):195–203.

Capitelli, M., Ferreira, C., Gordiets, B., and Osipov, A. (2000a). *Plasma Kinetics in Atmospheric Gases*. Springer, Berlin.

Capitelli, M., Gorse, C., and Longo, S. (2000b). Collision integrals of high temperature air species. *Journal of thermophysics and heat transfer*, 14(2):259–268.

Carlson, A. and Hassan, H. (1992). Direct simulation of re-entry flows with ionization. *Journal of Thermophysics and Heat Transfer*, 6(3):400.

Daiss, A., Fruhauf, H., and Messerschmid, E. (1997). Modeling of catalytic reactions on silica surfaces with consideration of slip effects. *Journal of Thermophysics and Heat Transfer*, 11(3):346.

Deutschmann, O., Riedel, U., and Warnatz, J. (1995). Modeling of nitrogen and oxygen recombination on partial catalytic surfaces. *Journal of Heat Transfer*, 117:495.

Doering, J. (1992). The atomic oxygen (p-3)-(d-1) electron-excitation cross section near threshold. *Geophysical Research Letters*, 19:449.

Doering, J. and Gulcicek, E. (1989a). Absolute differential and integral electron excitation cross section for atomic oxygen 7. the and transitions from 4.0 to 30 ev. *Journal of Geophysical Research*, 94:1541–1546.

Doering, J. and Gulcicek, E. (1989b). Absolute differential and integral electron excitation cross sections for atomic oxygen. viii - the 3p - 5s0 transition (1356 a) from 13.9 to 30 ev. *Journal of Geophysical Research*, 94:2733–2736.

Doering, J., Gulcicek, E., and Vaughan, S. (1985). Electron impact measurement of oscillator strengths for dipole-allowed transitions of atomic oxygen. *Journal of Geophysical Research*, 90:5279–5284.

Drawin, H. and Emard, F. (1973). Atom-atom excitation and ionization in shock waves of the noble gases. *Physics Letters*, 43A(4):333.

Dunn, M. and Kang, S.-W. (1973). Theoretical and experimental studies of reentry plasmas. Technical report, NASA CR-2232.

Dunn, M. and Lordi, J. (1969). Measurement of electron temperature and number density in shock-tunnel flows. part ii: $no^+ + e^-$ dissociative recombination rate in air. *AIAA Journal*, 7(11):2099.

Fuhr, J. and Wiese, W. (1990). *CRC Handbook of Chemistry and Physics*, pages 128–179. CRC Press, Boca Raton, FL.

Gomès, A., Essoltani, A., and Bacri, J. (1990). Collisional-radiative modelling of a non-equilibrium stationary oxygen plasma at atmospheric pressure, te= 3000-18,000 k. *Journal of Quantitative Spectroscopy and Radiative Transfer*, 43:471–498.

Gryzinski, M. (1965). Two particle collisions ii. coulomb collisions in the laboratory system of coordinates. *Physical Review A*, 138:322–335.

Gryzinski, M. and Kunc, J. (1986). Collisional ionization and the atomic model. *Journal of Physics B: Atomic, molecular and Optical Physcis*, 19:2479–2504.

Guberman, S. (2003). *Dissociative recombination of molecular ions with electrons*. Kluwer, Dordrecht.

Gulcicek, E. and Doering, J. (1988). Absolute differential and integral electron excitation cross sections for atomic oxygen. v - revised values for the 3p - 3s0 (1304 a) and 3p - 3d0 (989 a) transitions below 30 ev. *Journal of Geophysical Research.*, 93:5879–5884.

Gulcicek, E., Doering, J., and Vaughan, S. (1988). Absolute differential and integral electron excitation cross sections for atomic oxygen. vi - the 3p - 3p and 3p - 5p transitions from 13.87 to 100 ev. *Journal of Geophysical Research*, 93:5885–5889.

Gunton, R. and Shaw, T. (1965). Electron-ion recombination in nitric oxide in the temperature range 196 to 358 k. *Physical Review*, 140(3A):A756.

Gupta, R., Yos, J., Thompson, R., and Lee, K. (1990). Calculations and curve fits of thermodynamic and transport properties for equilibrium air to 30000 k. Technical report, NASA RP1232.

Hankey, W. (1994). *Re-entry aerodynamics*. AIAA Education Series, Washington.

Hansen, C. (1968). Temperature dependence of the $no^+ + e^-$ dissociative recombination rate coefficient. *Physics of Fluids*, page 904.

Hellberg, F., Rosen, S., Thomas, R., Neau, A., Larsson, M., Petrignani, A., and van der Zande, W. (2003). Dissociative recombination of no^+: Dynamics of the $x^1\sigma^+$ and $a^3\sigma^+$ electronic states. *Journal of Chemical Physics*, 118(14):6250.

Herzberg, G. (1950). *Spectra of Diatomic Molecules*. John Wiley & Sons, New York.

Hindmarsh, A. (1980). Lsode and lsodi, two new initial value ordinary differential equation solvers. *ACM SIGNUM Newsletter*, 15:10.

Holstein, T. (1947). Imprisonment of resonance radiation in gases. *Physical Review*, 72(12):1212.

Huang, C.-M., Biondi, M., and Johnsen, R. (1975). Variation of electron-no^+ recombination coefficient with electron temperature. *Physical Review A*, 11(3):901.

Itikawa, Y. and Ichimura, A. (1990). Cross sections for collisions of electrons and photons with atomic oxygen. *Journal of Physical and Chemical Reference Data*, 19:637.

Jumper, E. and Seward, W. (1994). Model for oxygen recombination on reaction-cured glass. *Journal of Thermophysics and Heat Transfer*, 8(3):460.

Kim, Y.-K. and Desclaux, J.-P. (2002). Ionization of carbon, nitrogen and oxygen by electron impact. *Physical Review A*, 66:012708.

Kley, D., Lawrence, G., and Stone, E. (1977). The yield of $n(^2d)$ atoms in the dissociative recombination of no^+. *Journal of Chemical Physics*, 66(9):4157.

Kolesnikov, A. (1999). Combined measurements and computations of high enthalpy and plasma flows for determination of tpm surface catalycity. In *Measurement techniques for high enthalpy plasma flows*, Belgique. von Karman Institute for fluid dynamics, RTO EN 8, NATO.

Kolodziej, P. and Stewart, D. (1987). Nitrogen recombination on high-temperature reusable surface insulation and the analysis of its effects on surface catalysis. AIAA Paper 87-1637.

Kossyi, I., Kostinsky, A., Matveyev, A., and Silakov, V. (1992). Kinetic scheme of the non-equilibrium discharge in nitrogen-oxygen mixtures. *Plasma Sources Science and Technology*, 1:207.

Kovalev, V. and Suslov, O. (1996). Simulation of the interaction between partially ionized air and the catalytic surface of high temperature reusable thermal insulation. *Fluid Dynamics*, 31(5):775.

Kunc, J. and Soon, W. (1989). Collisional radiative nonequilibrium in partially ionzed atomic nitrogen. *Physical Review A*, 40(10):5822–5842.

Laher, R. and Gilmore, F. (1990). Updated excitation and ionization cross sections for electron impact on atomic oxygen. *J. Phys. Chem. Ref. Data*, 19(1):277–305.

Laux, C. and Kruger, C. (1992). Arrays of radiative transition probabilities for the n_2 first and second positive, *no* beta and gamma, n_2^+ first negative and o_2 schumann-runge band systems. *Journal of Quantitative Spectroscopy and Radiative Transfer*, 48(1):9.

Losev, S., Makarov, N., Pogosbekyan, M., and Shatalov, O. (1994). Aiaa 94-1990. In *Proceedings of the American Institute of Aeronautics and Astronautics, 6th AIAA/ASME Joint Thermophysics and Heat Transfer Conference*, Washington,DC. AIAA 94-1990, American Institute of Aeronautics and Astronautics.

Losev, S. and Shatalov, O. (1990). Elaboration of computer data bank for physicochemical gasdynamics. *Soviet Journal of Chemical Physics*, 6(12):3299.

Lotz, W. (1968). Electron-impact ionization cross sections and ionization rate coefficients for atoms and ions from hydrogen to calcium. *Zeitschrift fur Physik*, 216(3):241.

Moore, C. (1993). *Tables of Spectra of Hydrogen, Carbon, Nitrogen, and Oxygen Atoms and Ions*, pages 203–209. CRC Press, Boca Raton, FL.

Motapon, O., Fifirig, M., Florescu, A., Waffeu-Tamo, F.-O., Crumeyrolle, O., Varin-Bréant, G., Bultel, A., Vervisch, P., Tennyson, J., and Schneider, I. (2006). Reactive collisions between electrons and no^+ ions: rate coefficient computations and relevance for the air plasma kinetics. *Plasma Sources Science and Technology*, 23(15):23–32.

Nasuti, F., Barbato, M., and Bruno, C. (1996). Material-dependent catalytic recombination modeling for hypersonic flows. *Journal of Thermophysics and Heat Transfer*, 10(1):131–136.

Nussbaumer, H. and Storey, P. (1983). Dielectronic recombination at low temperatures. *Astronomy and Astrophysics*, 126:75–79.

Park, C. (1969). Collisional ionization and recombination rates of atomic nitrogen. *AIAA Journal*, 7(8):1653–1654.

Park, C. (1971). Electron-impact excitation rate coefficients for hydrogen, helium and alkali atoms. *Journal of Quantitative Spectroscopy and Radiative Transfer*, 11:7–36.

Park, C. (1985). *Problems of rate chemistry in the flight regime of aeroassisted orbital transfer vehicles*, page 511. AIAA, New York.

Park, C. (1990). *Non-Equilibrium Hypersonic Aerothermodynamics*. Wiley, New York.

Park, C. (1993). Review of chemical-kinetic problems of future nasa missions, i: Earth entries. *Journal of Thermophysics and Heat Transfer*, 7(3):385.

Peterson, J., Le Padellec, A., Danared, H., Dunn, G., Larsson, M. Larson, A., Peverall, R., Strömholm, C., Rosen, S., af Ugglas M., and van der Zande, W. (1998). Dissociative recombination and excitation of n_2^+: Cross sections and product branching ratios. *Journal of Chemical Physics*, 108(5):1978.

Peverall, R., Rosen, S., Peterson, J., Larsson, M., Al-Khalili, A., Vikor, L., Semaniakand, J., Bobbenkamp, R., Le Padellec, A., Maurellis, A., and van der Zande, W. (2001). Dissociative recombination and excitation of o_2^+: Cross sections, product yields and implications for studies of ionospheric aifglows. *Journal of Chemical Physics*, 114(15):6679.

Pradhan, A. (1988). *Atomic Processes in Plasmas*. Academic, New York.

Sarrette, J.-P., Gomes, A.-M., Bacri, J., Laux, C., and Kruger, C. (1995). Collisional-radiative modelling of quasi-thermal air plasmas with electronic temperatures between 2000 and 13000 k -i. $\theta_e > 4000\,k$. *Journal of Quantitative Spectroscopy and Radiative Transfer*, 53(2):125.

Scott, C. (1990). Catalytic recombination of nitrogen and oxygen on high temperature reusable surface insulation. In *Aerothermodynamics and planetary entry*, New York. AIAA, Progress in Astronautics and Aeronautics.

Smith, A., Caplinger, E., Neynaber, R., Rothe, E., and Trujillo, S. (1962). Electron impact ionization of atomic nitrogen. *Physical Review*, 127:1647–1649.

Soon, W. and Kunc, J. (1990). Thermal nonequilibrium in partially ionized atomic oxygen. *Physical Review A*, 41(2):825–842.

Soon, W. and Kunc, J. (1991). Kinetics and continuum emission of negative atomic ions in partially ionized plasmas. *Physical Review A*, 43(2):723–734.

Sun, H. and Nakamura, H. (1990). Theoretical study of the dissociative recombination of no^+ with slow electrons. *Journal of Chemical Physics*, 93(9):6491.

Suslov, O. and Tirskyi, G. (1994). the kinetics of the recombination of nitrogen atoms on high temperature reusable surface insulation in hypersonic thermochemical non-equilibrium flows. In *2nd Europ. symp. on Aerothermodynamics for Space Vehicles*, Noordwijk, The Netherlands. ESTEC, ESA.

Sutton, K. and Gnoffo, P. (1998). Multi-component diffusion with application to computational aerothermodynamics. In *7th AIAA/ASME Joint Thermophyscis and Heat transfer conference*. AIAA Paper 98-2575.

Tawara, H. and Kato, M. (1999). Electron impact data for atoms and ions: up-dated in 1998. *NIFS Data Serie S*, 51:256P.

Tayal, S. and Henry, R. (1989). Oscillator strengths and electron collisional excitation cross sections for atomic oxygen. *Physical Review A*, 39(9):4531–4536.

Taylor, R. and Ali, A. (1986). Saha decrements and collisional-radiative recombination and ionization coefficients for a nonequilibrium oxygen plasma. *Journal of Quantitative Spectroscopy and Radiative Transfer*, 36:373–383.

Teulet, P., Sarrette, J.-P., and Gomes, A.-M. (1999). Calculation of electron impact inelastic cross sections and rate coefficients for diatomic molecules. *Journal of Quantitative Spectroscopy and Radiative Transfer*, 62:549.

Teulet, P., Sarrette, J.-P., and Gomes, A.-M. (2001). Collisional-radiative modelling of one- and two- temperature air and air-sodium plasmas at atmospheric pressure with temperatures of $2000 - 12000\,k$. *Journal of Quantitative Spectroscopy and Radiative Transfer*, 70:159.

Vejby-Christensen, L., Kella, D., Pedersen, H., and Andersen, L. (1998). Dissociative recombination of no^+. *Physical Review A*, 57(5):3627.

Verner, D., Verner, E., and Ferland, G. (1996). Atomic data for permitted resonance lines of atoms and ions from h to si, and s, ar, ca and fe. *Atomic Data Nucl. Data Tables*, 64:1.

Weller, C. and Biondi, M. (1968). Recombination, attachment and ambipolar diffusion of electrons in photo-ionized *no* afterglows. *Physical Review*, 172:198.

Wiley, R. (1993). Comparison of kinetic models for atom recombination on high temperature reusable surface insulation. *Journal of Thermophysics and Heat Transfer*, 7(1):55.